Imperial College of Science, Technology and Medicine
Solid State Experimental Research Group
Department of Physics, Blackett Laboratory
Prince Consort Road, London SW7 2AZ
M.Sc. Course in Semiconductor Science & Technology

LIGHT TRAPPING IN MQW SOLAR CELLS

Lars Steinke*

September 1996

*Fakultät für Physik der Albert-Ludwigs-Universität,
Hermann-Herder-Str. 3, D-79104 Freiburg, Germany
<steinke@ciphp01.physik.uni-freiburg.de>

Abstract

In this work multi quantum well (MQW) solar cell efficiency enhancement by up to 2.5% was achieved by multi-pass well absorption using patterned substrates: A theoretical and experimental investigation of anisotropically etched structures most suitable for light trapping in $AlGaAs/GaAs$ MQW solar cell structures was carried through which established that growth on patterned substrates can result in high quality solar cell material with lightrapping properties if the problem of substrate absorption is addressed. By modelling, the latter has been shown to be due to free carriers and a second absorption process, which most likely can be attributed to inter-valley scattering.

Keywords:

quantum well, solar cell, patterned substrate, free carrier absorbtion

Contents

List of Figures

List of Tables

Abbreviations & Acronyms

III-V — *Group III-V Semiconductors*

BEI — *Backscattered Electron Image*

CL — *Cathodoluminescence*

DI — *deionized*

EPSRC — *Engineering and Physical Sciences Research Council*

I-V — *Current-Voltage*

ICSTM — *Imperial College of Science, Technology & Medicine*

IRC — *Interdisciplinary Research Centre*

MBE — *Molecular Beam Epitaxy*

PECVD — *Plasma enhanced Chemical Vapour Deposition*

QE — *Quantum Efficiency*

(M)QW — *(Multi) Quantum Well*

QWSC — *Quantum Well Solar Cell*

p-(i-)n — *positively doped-(intrinsic-)negatively doped*

SEI — *Secondary Electron Image*

SEM — *Scanning Electron Microscope*

SMU — *Source Measurement Unit*

SR — *Spectral Response*

TCRC — *Toshiba Cambridge Research Centre*

UNSW — *University of New South Wales, Australia*

CHAPTER 1

Introduction

1.1 Background

The World's hunger for energy is ever growing as it is one of the decisive factors for our standard of living. For instance the present tendency to establish a "virtual" society apart from all its social implications means that more and more every day actions will heavily rely on electricity.

Our main source of energy, fossil fuels, will run out eventually, even with vast new oil and coal resources being explored constantly. The working alternative, atomic fission, involves the serious problems of safety and waste management and other alternatives like hot fusion are still in prototype stage and it has yet to be resolved whether cold fusion will ever yield energy for the masses.

Apart from wind and tidal energy, the Sun has great potential to provide Earth's population with energy, flaring off 1373 $\frac{W}{m^2 \cdot nm}$ spectral irradiation (at the distance Sun-Earth before passing through the atmosphere). This is tantamount to 100 $\frac{W}{m^2}$ power density available in the south-east U.K. in the year's average, a power supply of 900 $\frac{kWh}{m^2}$ per year. The problem is to gain access to this potential at reasonable cost: Biological conversion involving photo-synthesis with a conversion efficiency[1] reaching 90% seems like the perfect solution, which we are using indirectly at present burning up our fossil fuels. Unfortunately biochemists have yet a long way to go to actually "grow" a dedicated photosynthetical converter to satisfy our energy needs but an organic solar cell promises the cheapest solar energy conversion possible.

So, in the meantime, there are a quite a lot of other more practical (but more expensive) schemes around which aim for solar energy conversion at much lower conversion efficiencies, for instance electro-chemical cells absorbing photons in dyes with

[1] for light hitting the light harvesting complex

$\sim$10% efficiency and injecting photo-generated carriers into semiconductor material (Ref. [Grätzel and Bonhôte, 1994]). The highest efficiencies in photon conversion so far have been attained using photonic carrier-pair excitation across the bandgap in semiconductor solar cells which is the subject of this thesis.

Quantum Well Solar Cells (QWSC's) are a novel approach to the enhancement of solar cell efficiency above the theoretical limit of $\sim$43% for single bandgap cells ([Brendel et al., 1996]), taking into account hot electron excitation. This limit is mainly due by the mismatch of the broad solar spectrum shown in Fig. 1.1 to the narrow spectral response[2] of a single bandgap cell. As for tandem cells one employs the approach of using materials of different band-gaps to enhance the spectral response of a cell: While in tandem cells this is achieved by connecting two cells of different bandgap back to back[3], a QWSC features an intrinsic region (i-region) made up of thin quantum layers of alternating low and high bandgap semiconductors grown epitaxially (as seen in Fig. 1.2). The most common material system for growing such structures is $Al_xGa_{1-x}As$ as barrier-material and $GaAs$ for the wells but other combinations[4] grown by various epitaxial methods from different sources have been studied by the QWSC group at Blackett Lab, ICSTM (Ref. [Zachariou et al., 1996] & [Barnham et al., 1994]).

In any of these structures photons of energy below the high band-gap of the barrier-material but above the bandgap of the well material excite electron-hole pairs in the lower gap wells which are released thermally into the barrier-material (see 1.2). As shown by the QWSC group (Ref. [Barnham et al., 1994]) the photo-generated short circuit current I_{sc} is thus enhanced above that of a control cell with an i-region composed solely of the barrier material. Furthermore the enhancement of the open circuit voltage V_{oc} over a cell made of the well material has been shown (Ref. [Barnham et al., 1996]) to be more than expected from the shift of absorption edge. Hence it has been established that efficiency superior to single-gap cells can be

[2] a value denoting the conversion capabilities of a cell at given wavelength, see Chapter 4
[3] which inherently bears the problem of ensuring current continuity across the cell interface
[4] like lattice-matched $InP/InGaAs$ or strained $GaAs/InGaAs$

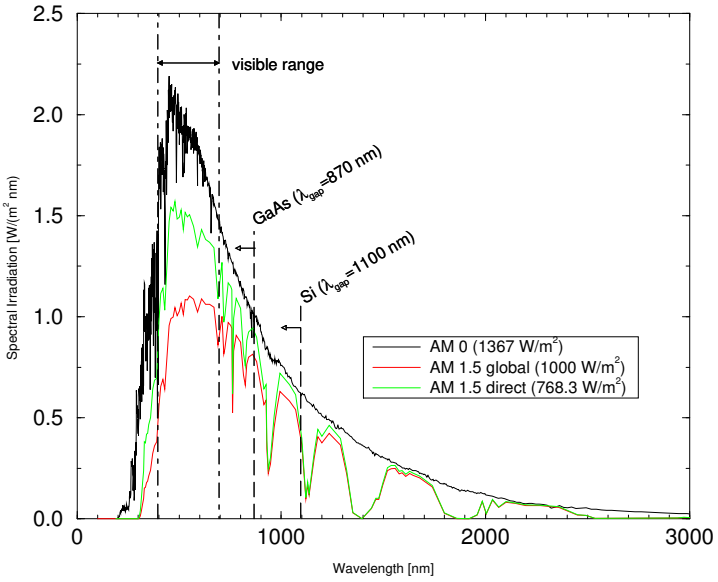

Fig. 1.1: The solar spectrum for different air masses (AM$\doteq cos(\theta)^{-1}$): AM 0 denotes the extraterrestrial spectrum, AM 1.5 the one after passing through the atmosphere at $\theta = 48°$ inclination. Apart from the overall attenuation the atmospheric absorption bands can be seen for AM 1.5, the global spectrum takes into account direct and diffuse irradiation

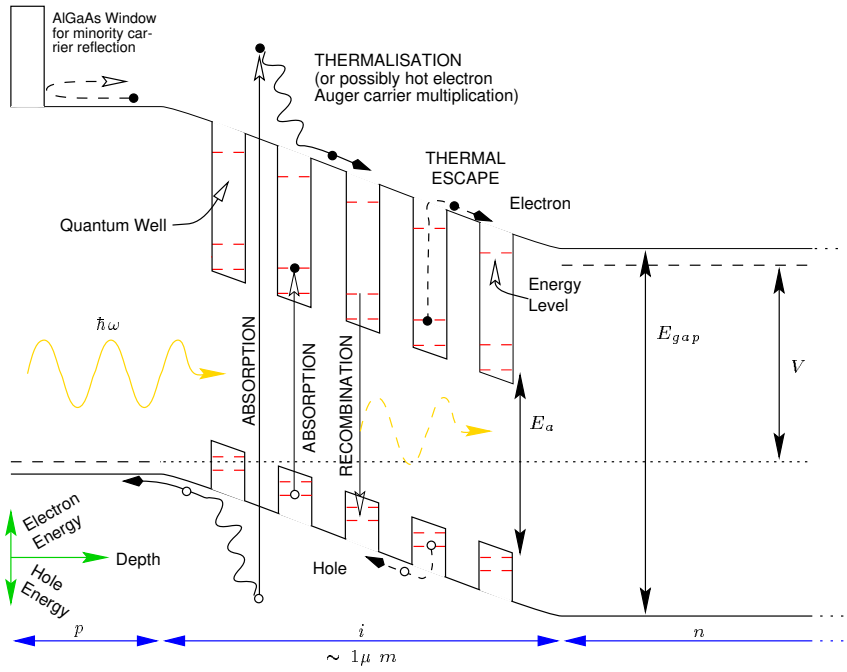

Fig. 1.2: Schematic structure of a Quantum Well Solar Cell

achieved with QWSC's in principle. It has to be mentioned though, that these cells suffer from material problems which account for moderate efficiencies[5] around 14% in $AlGaAs/GaAs$, well below the 29.5% world record efficiency tandem $GaInP/GaAs$ cell (Ref. [Green et al., 1996]). The most recent $GaAs/InGaAs$ devices have raised the maximum QWSC efficiency to $\sim 18\%$ (compared to a 20% efficient $GaAs$ control cell).

The object of this study is to increase efficiency further by enhancing light absorption in the quantum wells: $GaAs$ quantum wells in $AlGaAs$ absorb around 1% of the incident photon intensity per photo-excited transition so that for 10 wells with two possible transitions each absorb only 20% of the light[6] for a single pass through the i-region. One possible approach to enhancing absorption below the barrier bandgap is to incorporate more and deeper wells, but this is problematic: While samples containing 30-50 wells of around 8 nm width have been grown, the electric field cannot be maintained across such a large i-region if the level[7] of background doping is around $10^{21}\ m^{-3}$.

Thus we can see that increasing well absorption by multiple light passes through the i-region is desirable for the $GaAs/Al_{1-x}Ga_xAs$ material system, although the wells are not as shallow as for some of the other material systems mentioned above. For instance in $GaAs/InGaAs$ even more efficiency enhancement can be expected for increasing the number of light passes. Most cost effective and also applicable to already grown structures is a mirror on the back of the cell, sending light through the wells for absorption a second time. This has been tried before in $GaAs/InGaAs$ but without the expected two-fold absorption enhancement for a metallic mirror on the back of the substrate on which the cell structure was grown (Ref. [Barnes, 1994]). For this reason an examination of the absorptive properties of $GaAs$ substrate was carried out in this work (Chapter 3).

[5] although higher V_{oc} has been achieved, the current suffered from severe non-radiative recombination losses in $AlGaAs$

[6] for energies above the highest of the two well transitions, for the wavelengths below it is only 10% from one transition

[7] usually introduced for reasons like impurities in the growth chamber or the base material

Furthermore the QW absorption could be increased even further if more than a second pass through the wells could be achieved: Light trapping is possible when total reflection at *GaAs*-air interfaces is exploited, so this is another subject investigated in this thesis (Chapter 2). This approach relies on patterned substrates instead of plane back mirrors as for light to be trapped, it has to traverse the structure at low angle to the top surface for total reflection. There were two possible methods accessible for achieving light trapping which were both tried out: Either growing a new cell on patterned substrate (Chapter 4) or patterning substrate after a cell has been grown on top of it (Chapter 5). Although it is possible in principle to pattern both, top and bottom cell surfaces, a decision was made against this for reasons given in Chapter 2.

1.2 Shockley's Equation applied to Solar Cells

This section contains a quick recapitulation of the assumptions made in Shockley's theory of diodes leading on to its application to solar cells and the limits in doing so:

1.2.1 Shockley's Theory of Diodes

Derivation of Shockley's equation

In Appendix A.1 the Law of Mass Action is derived, the symbols have their usual definitions (c.f. A.1):

$$\sqrt{n \cdot p} \doteq n_i = 2h^{-3}(2\pi K_B T)^{3/2}(m_h^* m_e^*)^{3/4} \cdot e^{-\frac{E_{Gap}}{2KT}} \tag{1.1}$$

Therefore for intrinsic semiconductors with $m_h^* = m_e^*$ it follows that $n = p = n_i$ and $E_F = E_{Gap}/2$ while in case of doped material the Fermi level is shifted which results in unbalanced carrier populations n_{cb} and p_{vb}:

$$n_{cb} = n_i \cdot e^{-\frac{E_F - E_F^i}{KT}} \tag{1.2}$$

$$p_{vb} = n_i \cdot e^{-\frac{E_F^i - E_F}{KT}} \tag{1.3}$$

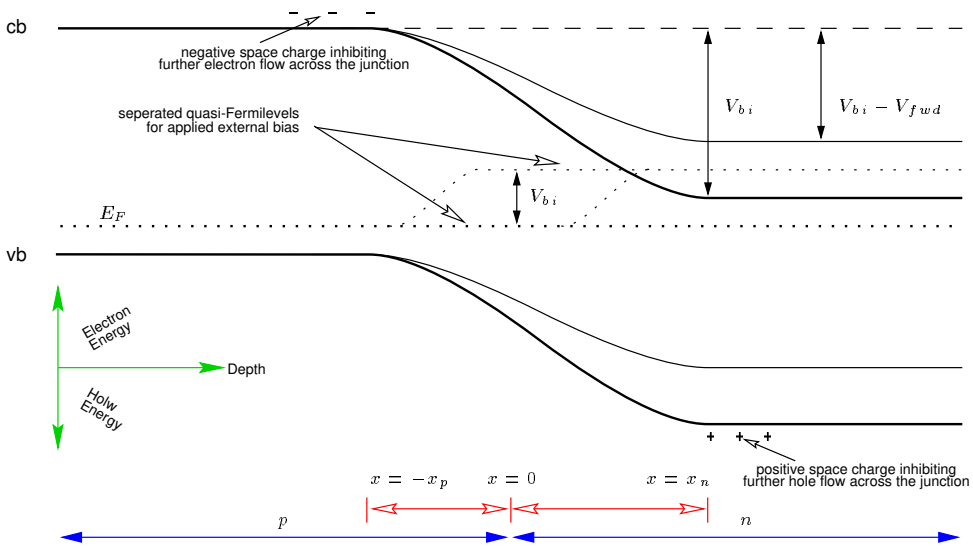

Fig. 1.3: Band energy scheme for a *p*-*n*-junction

If p- and n-doped material form a junction the two different Fermi levels align due to the equilibrium in the diffusion and drift components of the carrier flow so that a step of eV_{bi} is introduced into the band energy scheme (see Fig. 1.3) which leads to the following relation[8] for the minority carrier densities $n_{n/p0}$ & $p_{n/p0}$ on each side of the *p*-*n* junction in equilibrium:

$$n_{p0} = n_{n0} \cdot e^{-\frac{eV_{bi}}{KT}} \tag{1.4}$$

$$p_{n0} = p_{p0} \cdot e^{-\frac{eV_{bi}}{KT}} \tag{1.5}$$

If this equilibrium is disturbed by application of a bias the alignment of the Fermi levels[9] is suspended and the step increased or decreased by eV_{bias}. For forward bias Equations 1.2 & 1.3 imply for both sides of the junction:

$$n_n p_n = n_p p_p = n_i^2 \cdot e^{\frac{eV_{fwd}}{KT}}$$

From this we can deduce the effect of applied forward bias to be injection of minority carriers:

$$n_p = \frac{n_i^2}{p_p} \cdot e^{\frac{eV_{fwd}}{KT}} \text{ with } p_p \cong p_{p0} \overset{Eqn.1.4}{\Rightarrow} \frac{n_i^2}{p_p} \cong \frac{n_i^2}{N_A} \cong n_{p0} = n_{n0} \cdot e^{-\frac{eV_{bi}}{KT}}$$

[8] its derivation can be found in Appendix A.3
[9] now quasi-Fermi levels for p and n-type material respectively

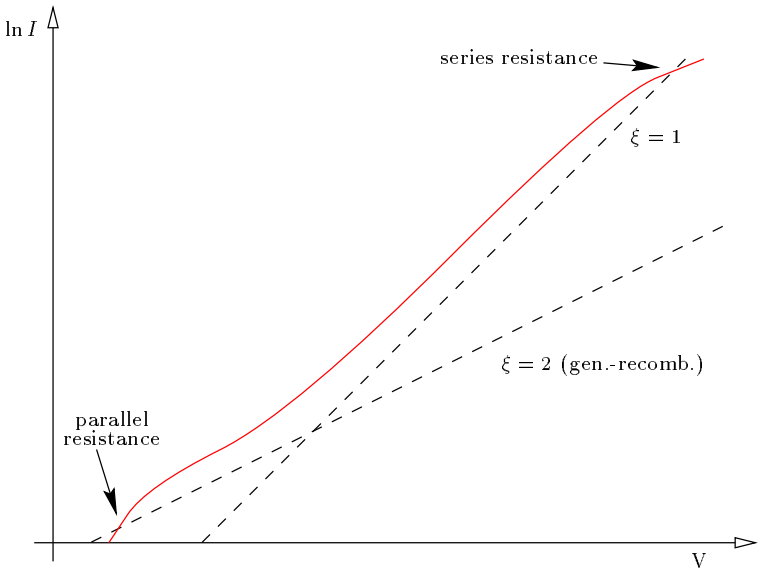

Fig. 1.4: Non-ideal diode characteristics

$$p_n = \frac{n_i^2}{n_n} \cdot e^{\frac{eV_{fwd}}{KT}} \text{ with } n_n \cong n_{n0} \overset{Eqn.1.5}{\Rightarrow} \frac{n_i^2}{n_n} \cong \frac{n_i^2}{N_D} \cong p_{n0} = p_{p0} \cdot e^{-\frac{eV_{bi}}{KT}}$$

The excess minority carriers $\Delta n/p = n/p_{p/n0} \cdot [\exp \frac{eV_{fwd}}{KT} - 1]$ recombine as they diffuse away from the respective depletion zone boundaries[10] to prevent buildup of charge in the material. The appropriate differential equation[11] for this process provides us with an exponential spatial decay of minority carriers outside the depletion region:

$$n_p(x) = n_{p0} + n_{p0} \cdot \left[e^{\frac{eV_{fwd}}{KT}} - 1 \right] \cdot e^{\frac{x+x_p}{\sqrt{\tau_e D_n}}} \quad \text{with } \sqrt{\tau_e D_n} \doteq L_n \tag{1.6}$$

$$p_n(x) = p_{n0} + p_{n0} \cdot \left[e^{\frac{eV_{fwd}}{KT}} - 1 \right] \cdot e^{-\frac{x-x_n}{\sqrt{\tau_h D_p}}} \quad \text{with } \sqrt{\tau_h D_p} \doteq L_p \tag{1.7}$$

As the electric field reaches 0 at the depletion zone boundaries the current densities $\vec{j_n} = eD_n \vec{\nabla} n + en\mu_n \vec{E}$, $\vec{j_p} = -eD_p \vec{\nabla} p + ep\mu_p \vec{E}$ can be estimated solely from the gradient of the carrier density there. Using this, Shockley's equation for the total current across the junction can be finally derived:

$$j = j_p|_{x=-x_p} + j_n|_{x=x_n} = e \left[\frac{n_i^2}{N_D} \cdot \sqrt{\frac{D_n}{\tau_e}} + \frac{n_i^2}{N_A} \cdot \sqrt{\frac{D_p}{\tau_h}} \right] \cdot \left(e^{\frac{eV_{fwd}}{KT}} - 1 \right) \tag{1.8}$$

[10] $-x_p$ & x_n
[11] c.f. Appendix A.4

The limits of Shockley's equation

The exponent $\frac{e}{1 \cdot KT}$ is achieved for ideal diodes only. To allow for effects causing deviation from this behaviour the ideality factor ξ is introduced so that the slope can be written $\frac{e}{\xi \cdot KT}$ for non-ideal regions of semi-logarithmic current-voltage characteristic plots like Fig. 1.4. The following effects cause deviation from Shockley's equation:

1. For low currents the effect of extinction and generation of carriers in the depletion zone will normally increase the current as non-ionised dopant sites or traps might release carriers. This generation-recombination region is very dominant for III-V semiconductors which is why we would expect to see an ideality factor of $\xi = 2$ for low forward bias (see [Nelson, 1995] Section D).

2. The resistance parallel to the junction might not be large enough to prevent leakage. Hence the actual diode is shunted at low forward bias which leads to resistive behaviour.

3. For high currents and accordingly low diode resistance the series resistance of the junction may have increasing effect, limiting the current to values below the Shockley prediction.

4. Similar behaviour to the series resistance can be observed, when Shockley's assumption of low minority carrier injection is invalidated at high current levels.

Typical diode behaviour demonstrating all these effects can be seen in Fig. 1.4.

1.2.2 Solar Cells

As a solar cell is a diode structure in forward bias under illumination we can apply the results of the preceding sections to it, switching from current densities j to currents I which are the measured values:

$$I = I_s \cdot \left(e^{\frac{eV_{fwd}}{KT}} - 1 \right) \text{ with } I_s = A \cdot e \left[\frac{n_i^2}{N_D} \cdot \sqrt{\frac{D_n}{\tau_e}} + \frac{n_i^2}{N_A} \cdot \sqrt{\frac{D_p}{\tau_h}} \right]$$

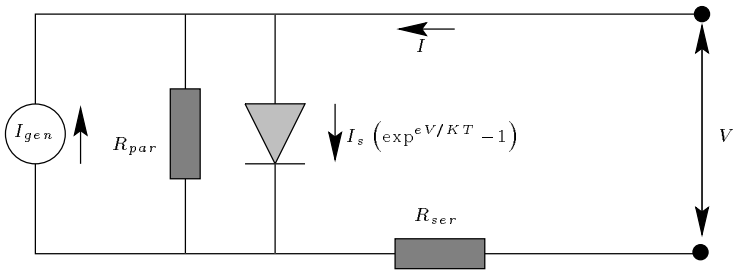

Fig. 1.5: Equivalent circuit for a non-idealised solar cell

And under Illumination:

$$I = I_s \cdot \left(e^{\frac{eV_{fwd}}{KT}} - 1 \right) - I_{gen}$$

Non-ideal solar cells

This characteristic applies to the ideal case but in reality we have to account for resistances as shown in the equivalent circuit Fig. 1.5 and also introduce an ideality factor ξ as mentioned in Section 1.2.1 to allow for recombination, non-radiative (involving impurities) and radiative (usually masked by the non-radiative one), which for $qV_{fwd} \gg KT$ results in:

$$V \longmapsto V - IR_{ser} \quad I_{gen} \longmapsto I_{gen} - \frac{V - IR_{ser}}{R_{par}}$$

$$\Rightarrow \qquad \ln\left(\frac{I + I_{gen} - \frac{V - IR_{ser}}{R_{par}}}{I_s} \right) = \frac{e}{\xi KT}(V - IR_{ser}) \tag{1.9}$$

Relation 1.9 provides us with a method for extracting I_s by extrapolating a logarithmic dark I-V-plot ($I_{gen} = 0$) from ∞ to $V = 0$.

Figures of merit

The maximum power a solar cell produces is given by $P_{max} = I_{max} \cdot V_{max}$ for $d(IV)/dV|_{V=V_m} = 0$. To measure the quality of energy conversion the fill-factor FF is introduced as

$$FF \doteq \frac{I_{max} V_{max}}{I_{sc} V_{oc}}$$

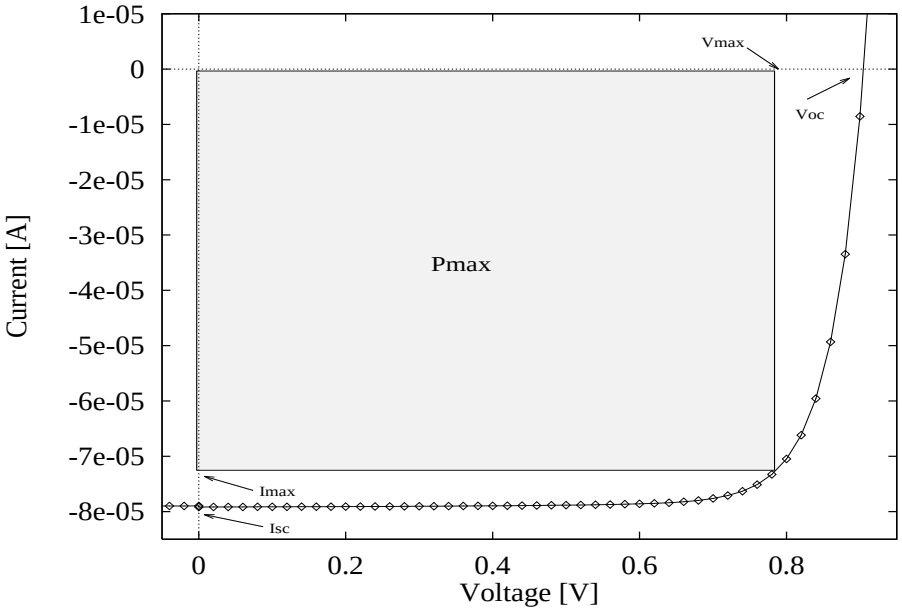

Fig. 1.6: Maximum power rectangle for a typical light I-V-characteristic

so we can define the conversion efficiency η:

$$\eta \doteq \frac{I_{max}V_{max}}{P_{in}} = \frac{FF \cdot I_{sc}V_{oc}}{P_{in}}$$

P_{in} is the incident light power; FF, I_{sc} & V_{oc} are high in a high efficiency cell, e.g $FF = 80 - 90\%$ depending on parallel and serial resistance while values of I_{sc},V_{oc} depend on area and bandgap of a cell (for an example see below).

Apart from I-V characterisation it's also important to study a solar cell's spectral response: Spectral response (SR) curves show what percentage of incoming photons at energy $\hbar\omega$ are converted to an $e-h$ pair, a value called quantum efficiency which is defined as $QE = \frac{j_{sc}(\lambda)}{qF(\lambda)}$ where j_{sc} is the short circuit current and F the incoming photon flux.

The figures of merit FF,V_{oc},I_{sc} can be found using the respective I-V characteristics for our cells at full intensity of a $(1230 \pm 3)\ W/m^2$ Tungsten light-source and a $2.30 \cdot 10^{-7} m^2$ $GaAs$ reference cell QT510c of 18% efficiency and an ideality factor of $\eta = 1.85$: Corrections can be made via integrating the product of measured SR and 3200 K black body spectrum[12] to give an efficiency in a 1000 W/m^2 AM 1.5 spectrum. The efficiency calculated in this way agreed within errors with

[12] which results in a corrected value for I_{sc}

actual measurements made on QT510 in the solar simulator at NREL. This gives us the possibility to use QT510's calibrated values for short circuit current (80.70 μA) and open circuit voltage (0.9286 V) to adjust the light intensity of the Tungsten source for recording light I-V characteristics of other cells at AM 1.5 conditions. Of course this works best for other $GaAs$ cells with similar spectral response but for completely different materials like for instance InP the method fails completely. As the measurements in this thesis are on $AlGaAs/GaAs$ cells the efficiencies obtained should be fairly close to AM 1.5.[13]

To illustrate the procedure, Figure 1.6 shows the maximum power rectangle for a typical dataset. While it can be determined graphically, in practice a program fits the maximum power rectangle to measured light I-V characteristics and then relates the maximum power to the one of the calibrated reference cell to calculate an AM 1.5 efficiency.

[13] the correction for a more realistic value for I_{sc} by integrating the product of spectral response and AM 1.5 spectrum over wavelength could be made but in this thesis we only look at efficiency values for direct comparison anyway

CHAPTER 2

Geometrical Considerations

2.1 Introduction

In the Introduction it was mentioned how light trapping can enhance the efficiency of MQW solar cells in particular. Work by M.A. Green [Green, 1987] suggests that a randomizing Lambertian back-reflector (which can be easily modelled[1]) would result in maximum light trapping for isotropic incidence of light.

In a solar cell with light of mainly perpendicular incidence it has been thought to be more effective though to use geometrical structures for light trapping. This has been shown to be true by Green's group using ray-tracing methods so that we chose to employ such geometrical structures which can be produced using anisotropic etching. The Toshiba Cambridge Research Centre Ltd. (TCRC) has used anisotropic etching with buffered *HF* to obtain grooves and dot shaped mesa- and vee-structures in *GaAs* which are shown in Figs. 4.1, 4.2 & 4.3. TCRC uses such processing for creating 0-dimensional electron gases when the side facets of a mesa are depleted using a back-gate field. Also, when a magnetic field is applied parallel to a wafer so that it is vertical to a ridge structure on top, interesting non-linear magnetic effects have been found experimentally.

Apart from geometrical light trapping it is also possible to make use of diffraction by producing a grating but the feature sizes achievable by TCRC's etching method (c.f. 4.1) are larger than the wavelengths of visible light[2] λ/n_{GaAs} in *GaAs*.

The growth structure of our cell designs relies on a thin p-region at the top surface of the cells. This is to make sure most of the light is absorbed on the i-region where light can be absorbed by bulk and QW's and generated electron-hole pairs are separated by the built-in junction field which is crucial for collection.

[1] c.f. Ref. [Yablonovitch and Cody, 1984]

[2] which account for most of the solar spectral irradiation as can be seen in Fig. 1.1.

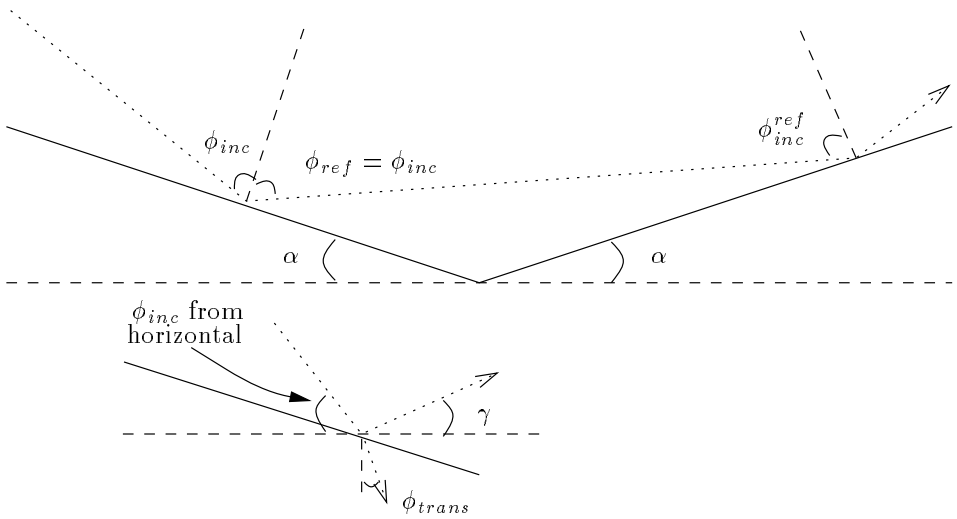

Fig. 2.1: Angle definitions used in Table 2.1

For this reason we could not use any top-processing approach like Green's grooves perpendicular to each other for top and back which have yielded best results for light trapping. Thus it was decided to pattern the back of the *p-i-n* structures and make use of total reflection from a flat top surface.

2.2 Total internal Reflection

2.2.1 Reflection from the Back

Using Fresnel's coefficients (see Appendix B on page 58) and the angle definitions as shown in Fig. 2.1 Table 2.2 was calculated and plotted as Fig. 2.2.

The table contains reflectivities R for the two polarisations of light calculated at different angles of incidence for a $GaAs$/air interface and indicates the direction of the reflected beam measured to the horizontal in the column for γ. In this chapter horizontal and vertical shall be defined in respect to the (100) surface of the wafer.

At the critical phase angle a material, in this case $GaAs$, changes its refractive behaviour to total internal reflection as indicated by the reflectivity approaching unity rapidly at $\phi_{ph} = 16.6°$ in Fig. 2.2.

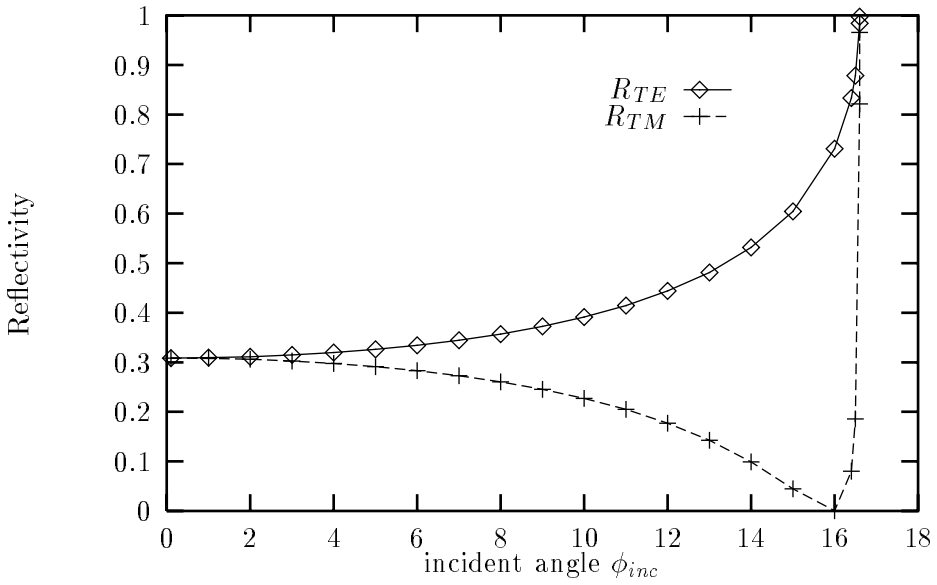

Fig. 2.2: Fresnel coefficients for $\alpha = 20°$ tilted $GaAs$ back-surface

For the wedge structure shown in the figure below this means a beam of grazing incidence from the right will be refracted at ϕ_{ph} from the normal (as light paths are reversible) and beams of higher inclination at even lower angles.

If the back surface was a mirror and tilted by ϕ_{ph} this results in the light being reflected back to the top surface at angles larger than ϕ_{ph} which is equivalent to the total reflection condition there. This remains true even more for incidence from the left.

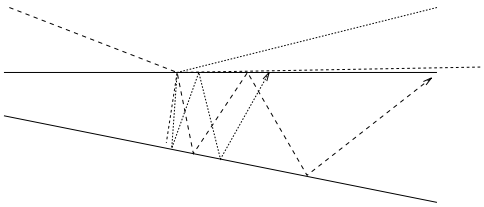

Fig. 2.3: Reflections from wedged back-surface for different angles of incidence on top-surface

2.2.2 Conclusions for Light Trapping

Thus we can deduce that a $\sim 16°$ tilted reflecting wedge on the back-surface will lead to light trapping for at least four passes through the structure for light of normal incidence. This angle has then been used in determining the side-angles for etching grooves and cones into substrate as $\sim 20°$ to allow for $\pm 5°$ errors arising from etchant composition.

It has to be noted though that, unlike for the wedge, for grooves and cones reflection at opposite surfaces can occur. This only occurs for incidence at low angles to the horizontal as Table 2.2 shows as well — light at around vertical incidence will be reflected away from an opposite surface which is signified by the relation $\gamma > \alpha$. Thus the pathological case of reflection to the opposite surface and directly out of the cell again won't occur for the dominant normal incidence.

Also from Table 2.2 & Fig. 2.2 we can see how for the back-surface all the light reaching the $GaAs$-air interface under angles ϕ_{inc} greater than ϕ_{ph} will be reflected back into the material totally. Therefore we can even make do without mirroring the patterned substrate: As we can assume that the light from a flat top surface will reach the back surface at $\phi_{inc} = 20°$ (at 20° tilt) for incidence of sunlight normal to the solar cell, total reflection from the back-surface will take place.

All these results are also applicable to $Al_{0.3}Ga_{0.7}As$-air interfaces as the change in refractive index[3] is minimal.

The reflection away from opposite surfaces for near normal incidence together with the total reflection at the top implies guaranteed four passes of light through the device as mentioned above.

The number of further passes can be calculated using Snell's law as before but as the geometry of the grooved systems is quite complicated and dependent on groove depth, this system has to be analysed properly using ray-tracing algorithms as was done by M. A. Green (Ref. [Green, 1987]) for Si. His results suggest that at optimal tilt for light trapping more than 4 passes are easily achieved for grooved or pyramidal structures. For all practical purposes in this work we can assume four passes to be sufficient to absorb all the light at quantum well wavelengths in a 25% absorptive 20-MQW structure.

[3] $n = 3.6$ for $GaAs$

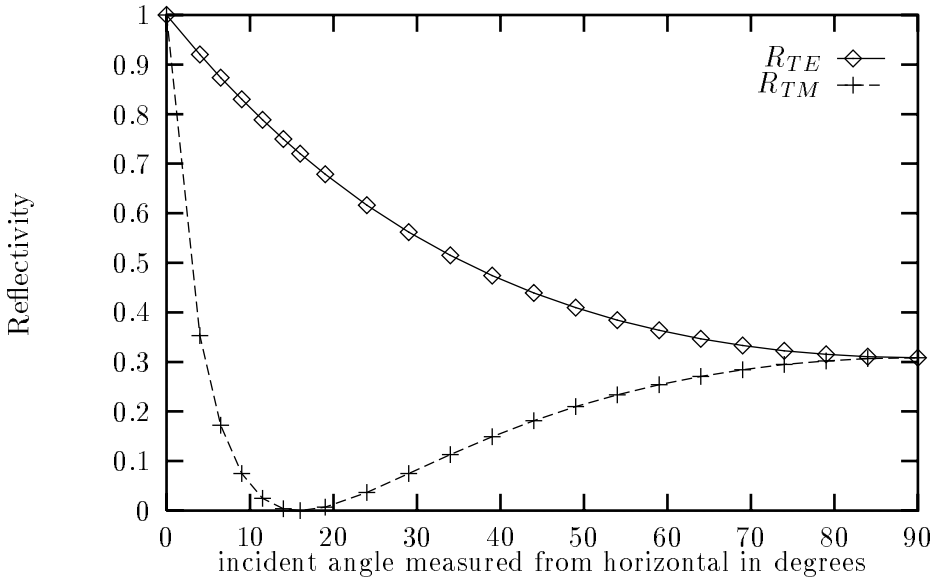

Fig. 2.4: Fresnel coefficients for a horizontal *GaAs* top-surface

2.3 Anti-reflective Coatings

A final look at the reflectivities of the top-surface shows us (Table 2.1 & Fig. 2.3) that we cannot make do without coating the devices with an anti-reflective (AR) layer:

For 16° incidence is under the Brewster angle, the angle of minimum reflection. Therefore this is the optimal incidence for coupling light into a solar cell. Although 100% transmission of TM polarised light is guaranteed under the Brewster condition, still 72% of the TE polarisation is reflected and thus never have the chance of being absorbed in the solar cell material. An AR coating is vital if this considerable percentage of incident light is not to be lost reflectively.

For a solar cell incidence is normal to maximise the cell area facing the sun, so that Brewster incidence could only be achieved for a top pattern of 74° inclination. In this work we have decided to avoid double patterning due to the brittleness of our samples and the structure of cells already grown, which only allows patterning on the back of samples. Therefore applying AR coatings is even more crucial for coupling light into the cells looked at in this thesis, as they lack the Brewster feature.

ϕ to (100)	ϕ_{inc}	ϕ_{inc} (RAD)	ϕ_{trans}	ϕ_{trans} (RAD)	R_{TE}	R_{TM}	γ
9.9998232e-11	90	1.5707963	16.60155	0.2897517	1	1	9.9998232e-11
4	86	1.5009832	16.559942	0.28902552	0.92018232	0.35282473	4
6.5	83.5	1.4573499	16.491773	0.28783575	0.87373593	0.17240542	6.5
9	81	1.4137167	16.391353	0.28608307	0.82986569	0.074695215	9
11.5	78.5	1.3700835	16.258921	0.2837717	0.78850199	0.025018745	11.5
14	76	1.3264502	16.094794	0.28090714	0.74956733	0.0039831817	14
16	74	1.2915436	15.940931	0.27822173	0.72011248	2.7345688e-06	16
19	71	1.2391838	15.673084	0.27354691	0.67864605	0.0070620718	19
24	66	1.1519173	15.130178	0.26407142	0.61638672	0.036795164	24
29	61	1.0646508	14.471083	0.25256804	0.56204426	0.07473102	29
34	56	0.97738438	13.701753	0.23914071	0.51487809	0.11325983	34
39	51	0.89011792	12.82898	0.22390795	0.47417766	0.14924099	39
44	46	0.80285146	11.860272	0.2070008	0.4392803	0.18147882	44
49	41	0.71558499	10.80374	0.18856084	0.40958254	0.20964448	49
54	36	0.62831853	9.667989	0.16873824	0.38454647	0.23378997	54
59	31	0.54105207	8.4620172	0.14769006	0.36370233	0.25412101	59
64	26	0.45378561	7.1951296	0.1255787	0.34664849	0.27088868	64
69	21	0.36651914	5.8768625	0.1025706	0.3330499	0.28433772	69
74	16	0.27925268	4.5169222	0.078835165	0.32263563	0.2946823	74
79	11	0.19198622	3.1251351	0.054543897	0.31519614	0.30209526	79
84	6	0.10471976	1.7114087	0.029869717	0.31058078	0.30670382	84
89.999999	1e-06	1.7453292e-08	2.8571428e-07	4.986655e-09	0.30864198	0.30864198	89.999999

Table 2.1: Reflectivities for a horizontal $GaAs$ top-surface

ϕ to (100)	ϕ_{inc}	ϕ_{inc} (RAD)	ϕ_{trans}	ϕ_{trans} (RAD)	R_{TE}	R_{TM}	γ
109.9	0.1	0.0017453293	0.350002	0.0061086873	0.30864856	0.30863539	69.9
109	1	0.017453293	3.5020024	0.061121472	0.3093014	0.30798262	69
108	2	0.034906585	7.0160998	0.12245404	0.31129544	0.30598973	68
107	3	0.052359878	10.554799	0.18421599	0.31467243	0.30261783	67
106	4	0.06981317	14.131469	0.24664065	0.31951666	0.29778781	66
105	5	0.087266463	17.760877	0.30998579	0.32595443	0.29138156	65
104	6	0.10471976	21.459879	0.37454555	0.33416401	0.28323335	64
103	7	0.12217305	25.248351	0.44066685	0.34439089	0.27311676	63
102	8	0.13962634	29.150535	0.50877281	0.35697177	0.26072502	62
101	9	0.15707963	33.197083	0.57939841	0.37237258	0.24564119	61
100	10	0.17453293	37.428334	0.65324766	0.39125149	0.22729208	60
99	11	0.19198622	41.899918	0.73129152	0.41456892	0.20487621	59
98	12	0.20943951	46.693163	0.81494944	0.44379476	0.17725075	58
97	13	0.2268928	51.93657	0.90646414	0.48134052	0.1427661	57
96	14	0.2443461	57.857405	1.0098022	0.53160757	0.099135767	56
95	15	0.26179939	64.940261	1.1334214	0.60423305	0.044509452	55
94	16	0.27925268	74.73768	1.3044186	0.7308047	0.0004497858	54
93.6	16.4	0.286234	81.187544	1.41699	0.83306884	0.080043778	53.6
93.5	16.5	0.28797933	83.748615	1.4616891	0.87823842	0.18588218	53.5
93.4	16.6	0.28972466	89.228247	1.5573267	0.98406538	0.821249	53.4
93.3985	16.6015	0.28975084	89.861929	1.5683865	0.99713029	0.96540712	53.3985

Table 2.2: Reflectivities for a grooved ($\alpha = 20°$) $GaAs$ back-surface

CHAPTER 3

Optical Measurements

3.1 Experimental Setup & Procedure

Studies on absorption in doped $GaAs$-substrate were carried out using the setup in Fig. 3.1 featuring two Bentham monochromators scanning the wavelength ranges $400 - 1100$ nm and $850 - 1650$ nm respectively. Transmission and reflection spectra were obtained using a PC for controlling the monochromator and lock-in amplifier through an IEEE-488 interface and relating the lock-in amplified solid state detector output to wavelength. For scanning the visible range a large area Si-detector was available while for the IR wavelengths up to 1700 nm a low bandgap material had to be used for detection. In this setup an $InGaAs$ detector of very high sensitivity was employed. The very small detection area of the latter unfortunately makes focusing a light spot on it difficult as high focal length lenses had to be used to make reflection measurements at angles very near 90° possible. Because of this the spectra taken using it differed noticeably from scan to scan, which was not the case with the Si detector.

3.2 Results

Transmission, reflection & resulting absorption ($\mathcal{R} + \mathcal{T} + \mathcal{A} = 1$, see Appendix B) of n-$GaAs$ are shown in Figs. 3.2 & 3.3 for the two monochromators as described in section 3.1. The IR reflectivity shows large spread in the spectra due to the small area $InGaAs$ detector used. Fig. 3.4 shows how the results for the two wavelength ranges match up.

To explain the below bandgap absorption in $GaAs$ the Drude-Zener model for free carrier absorption, which is derived in Appendix C, was used and the result is

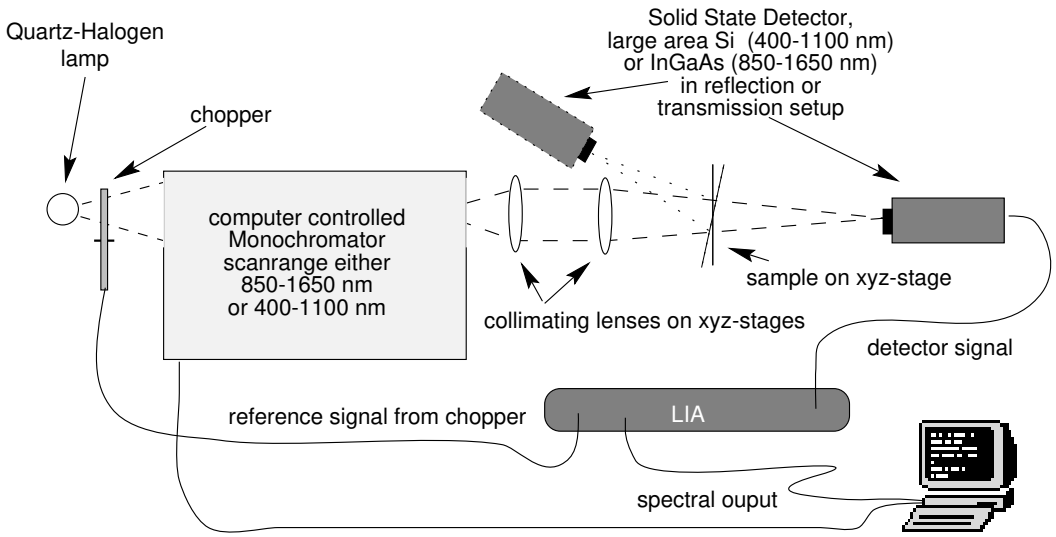

Fig. 3.1: Experimental setup

plotted in Fig. 3.5. The parameters used are thickness d, mobility μ and dopant density N which were provided by the characterisation unit of the EPSRC III-V Growth Facility in Sheffield. Remarkably the measured absorption in our substrate was much higher than predicted by the model (Fig. 3.6) and does not at all fit the spectral shape.

From this it must be deduced that another absorptive mechanism is present which should roughly have the inverse shape of the free carrier absorption calculated to account for the flat spectral shape of the measured absorption. One such mechanism could possibly be inter-valley scattering of electrons into the next higher conduction band minimum with a spacing of $25meV$ for $GaAs$ along $<111>$ (Ref. [Spitzer and Whelan, 1959]). The scattering process would definitely trail off for low energies/long wavelengths which satisfies the spectral shape condition stated above. This could not possibly be modelled in this thesis as going into $k \cdot p$ and scattering theory would be beyond scope. Even so it would have still been possible to check on the values (provided by the characterisation unit of the EPSRC III-V growth facility in Sheffield) for mobility μ, dopant concentration N and thickness d as used for the plot Fig. 3.6 if the experimental setup would have permitted probing wavelengths up to 4 or 5 μm where the absorption spectrum should have fitted the spectral shape of the now dominant free electron absorption.

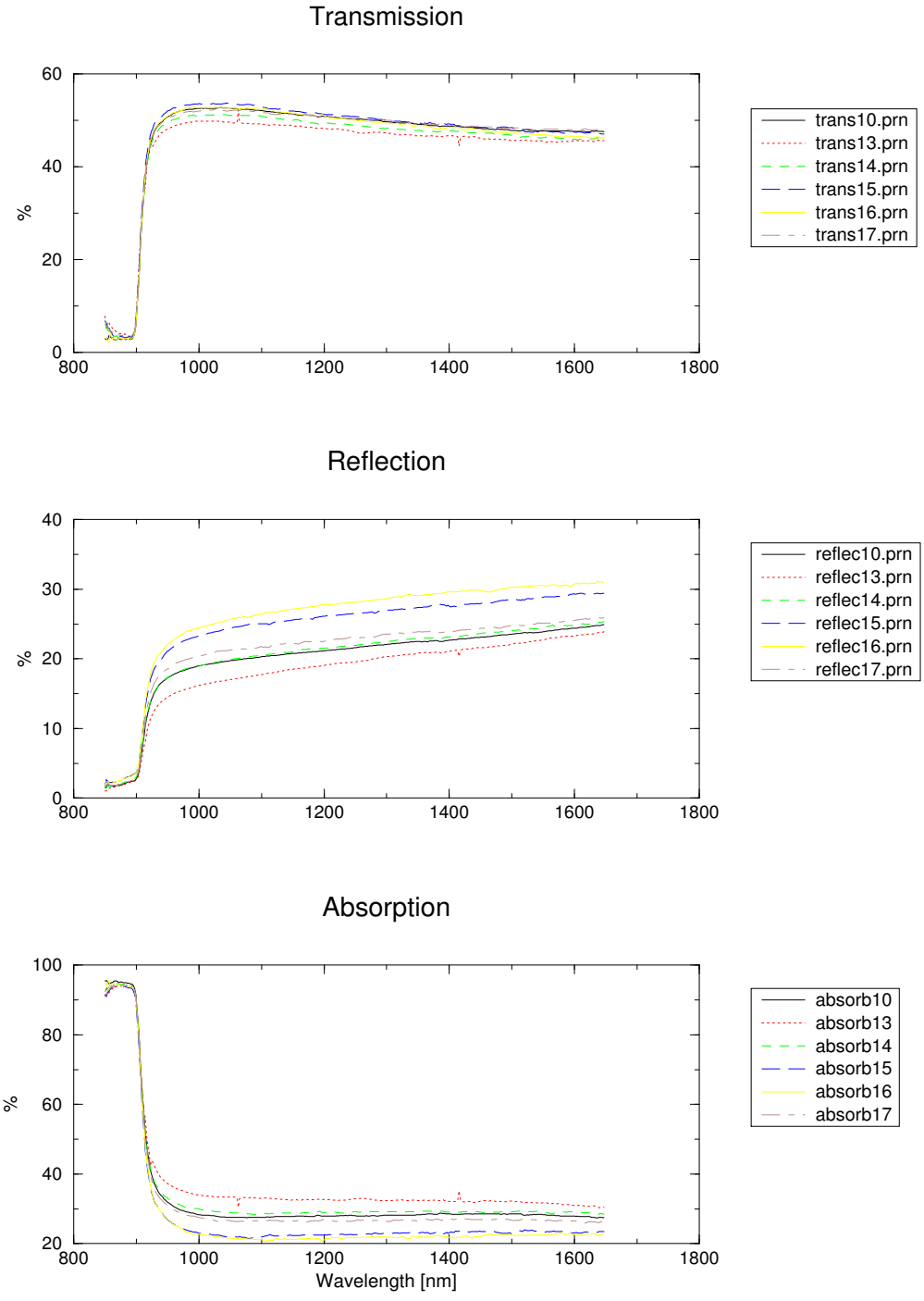

Fig. 3.2: Optical properties of GaAs-Substrate [850-1650 nm]

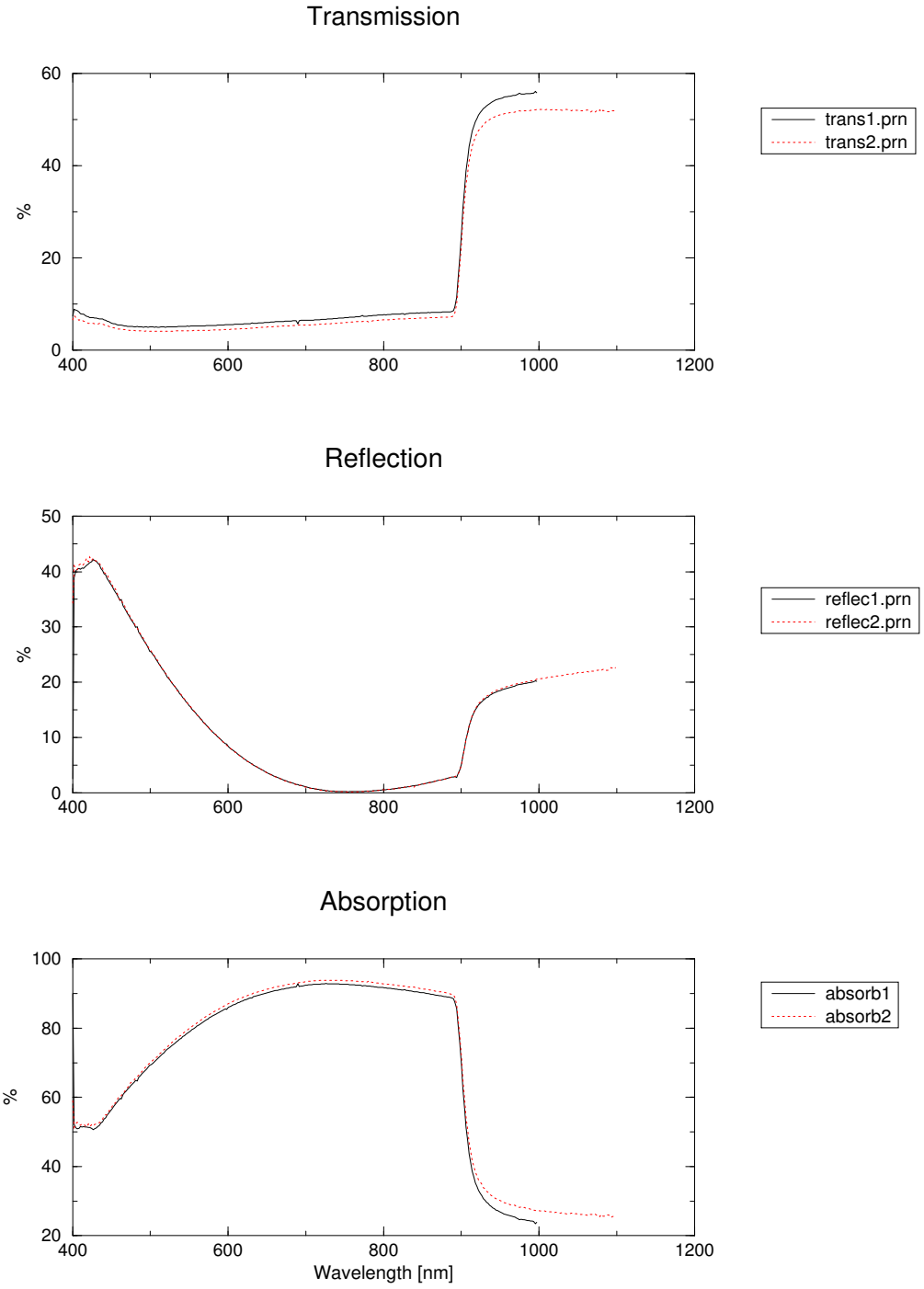

Fig. 3.3: Optical properties of GaAs-Substrate [400-1100 nm]

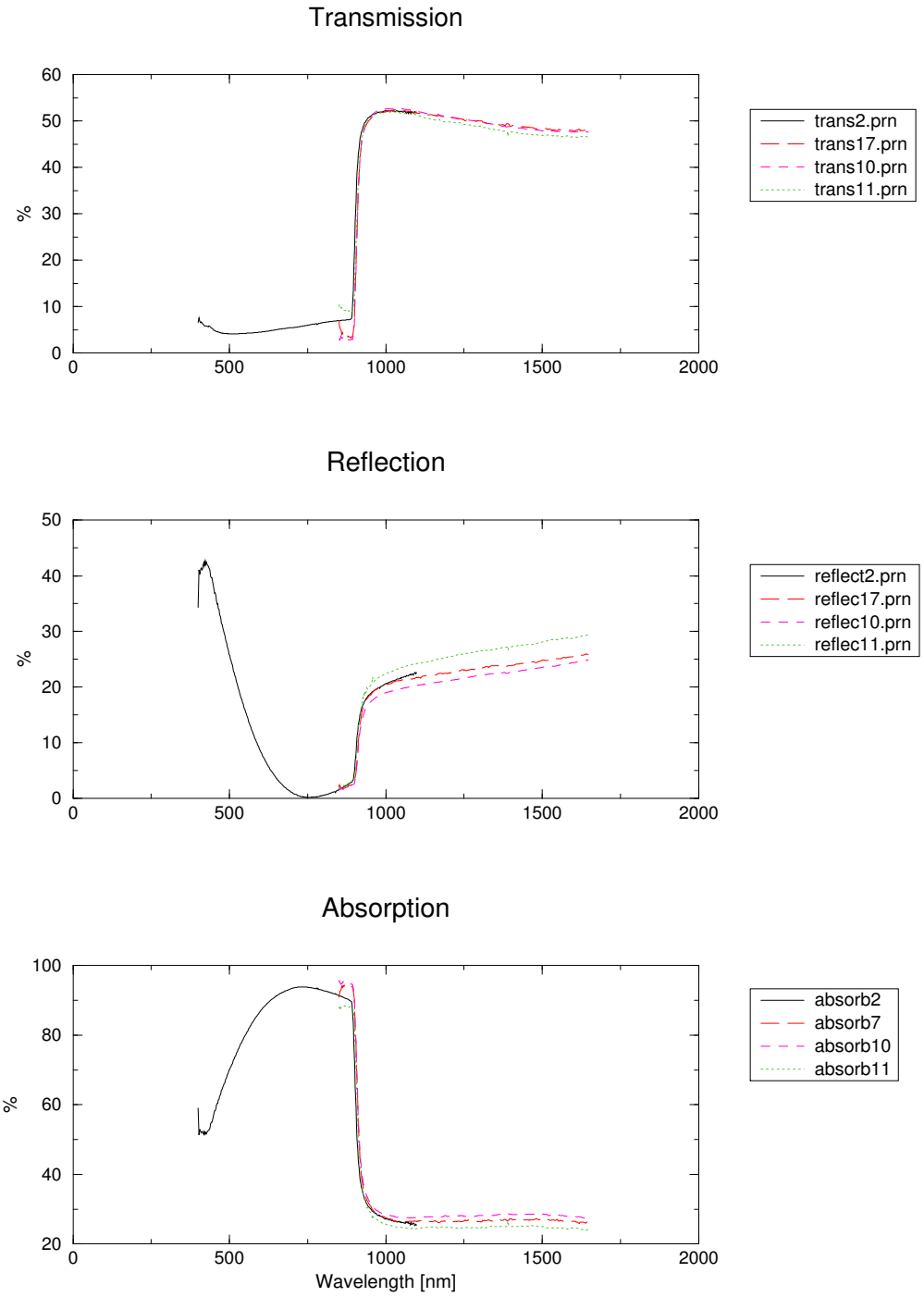

Fig. 3.4: Joint data for the wavelength intervals 400-1100 nm & 850-1650 nm

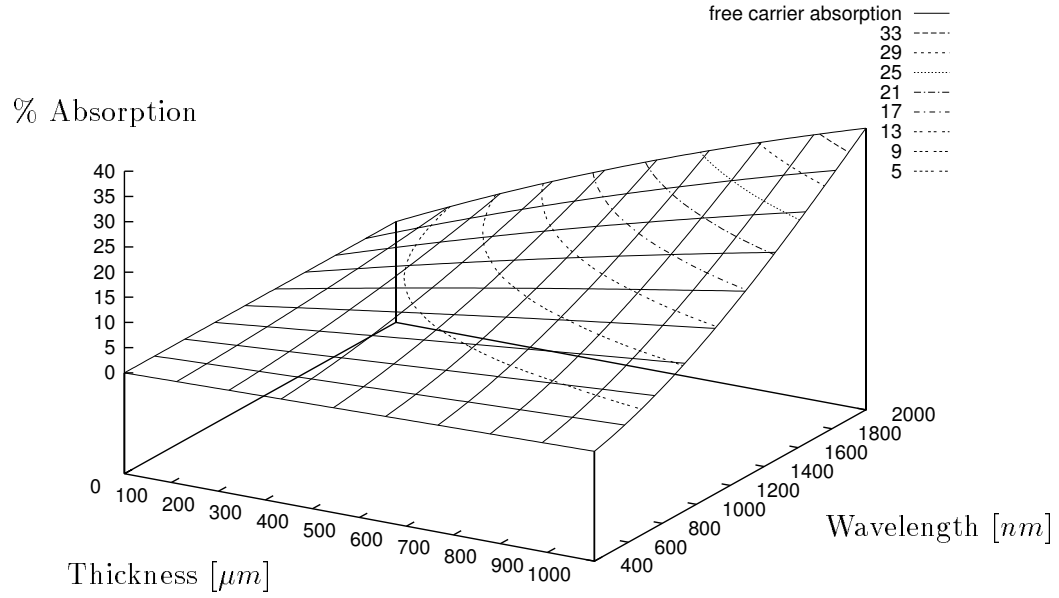

Fig. 3.5: Theoretical free carrier absorption in n-$GaAs$ substrate for $\mu = 0.3\ m^2/(Vs)$, $N = 1.0 \times 10^{24}\ m^{-3}$ at varying thicknesses and wavelengths

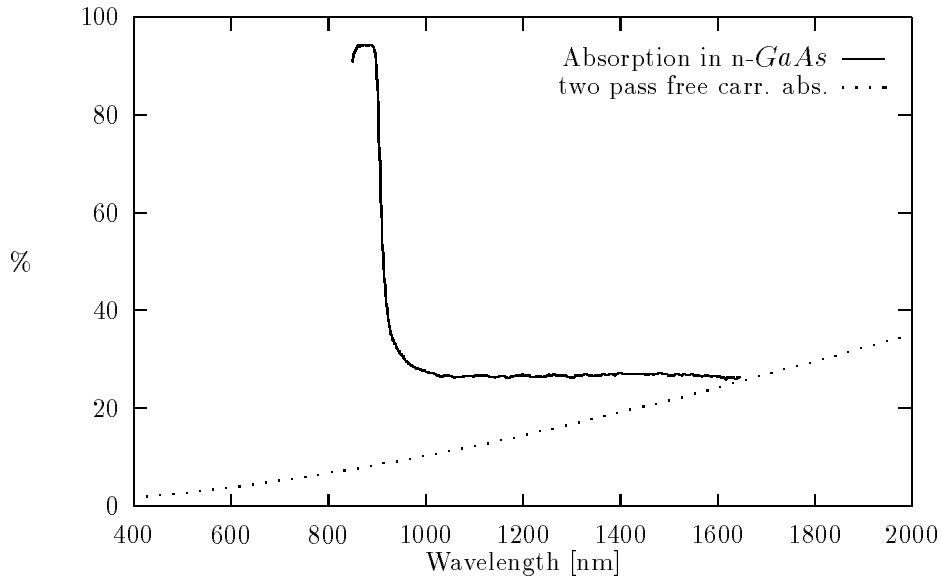

Fig. 3.6: Measured absorption in n-$GaAs$ substrate and theoretical free-carrier absorption for $\mu = 0.3\ m^2/(Vs)$, $N = 1.0 \times 10^{24}\ m^{-3}$, $d = 500\ \mu m$

3.3 Modelling

The model for the free-carrier absorption was next incorporated into a simple model aiming to understand why experimental data has not shown any enhancement in quantum efficiency (especially not for the below bandgap region around the QW energies) for an $GaAs/InGaAs$ QW cell with a plane mirror on its back.

The idea was to use the quantum efficiency (QE) data (which relates the current response of a cell to the spectrum it is illuminated with) for an un-mirrored cell and then try to make a modelled prediction whether the free carrier absorption could cancel out the light reflected from a back mirror before reaching the QW region again. The basic assumptions for an idealised starting model are shown in Fig. 3.7. From this the following calculations have been derived to be applied on the data. T signifies the transmitted fraction of photons, A the absorbed fraction:

$$T_{QW} + A_{QW} = 1 \text{ with } A_{QW} = QE \;\Rightarrow\; T_{QW} = 1 - QE$$

$$T_{sub} = T_{QW} \cdot (1 - A_{fc}) \text{ and } A_{enh} \doteq T_{sub} \cdot A_{QW}$$

$$\Rightarrow \quad A_{QW}^{mir} = A_{QW} + A_{enh} = QE + (1 - QE)(1 - A_{fc})A_{QW}$$

The result of modelling A_{QW}^{mir}, the quantum efficiency of QT459B A_{QW} enhanced by A_{enh}, the contribution from additional photons reflected by the mirror, is shown in Fig. 3.8. It is important to realize that this unsophisticated model will only be applicable for the QW absorption (wavelengths beyond the barrier band edge at 900 nm) as the assumption $A = QE$ only applies for the wells: In the bulk region a large percentage of photons absorbed will not contribute to the QE as they are lost in non-radiative recombination processes. Research in the QWSC group has shown that the probability of thermal escape from the wells at room temperature is close to 100%.

Not surprisingly the model predicts quite some substantial enhancement in quantum well QE which is not found in experiment. This shows us that free carrier absorption alone cannot account for the lack of mirror enhancement with the substrate left on the back of the cell. It rather seems that the second absorptive process, whose

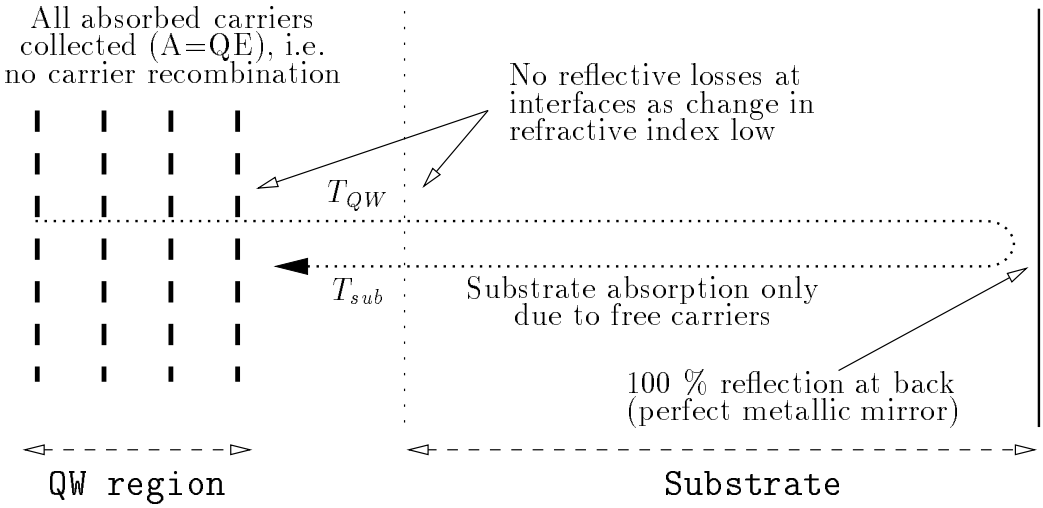

Fig. 3.7: Assumptions for modelling QE for a mirrored QWSC retaining its substrate

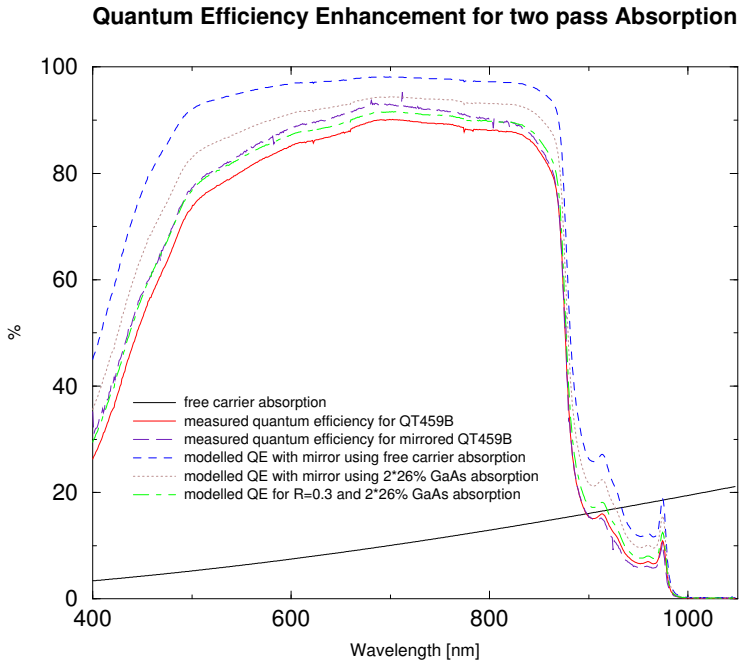

Fig. 3.8: Results for modelling QE for a mirrored QWSC retaining its substrate

tentative identification as inter-valley scattering has yet to be verified by modelling, has a non-negligible effect on suppressing second pass absorption in the quantum well region and clearly all the idealised assumptions about the absence of optical losses on the way to the mirror and back are far too optimistic.

To get a better feeling what the enhancement would be under more realistic assumptions, a second approach to modelling QE was made: The second modelled dataset shows the same calculation but using two times the constant 26% measured absorption[1] for one pass through *n-GaAs* (see Fig 3.6) instead of free-carrier absorption only. This should also take into account all the optical effects the initial model didn't include. The result shows attenuation for the QW region due to the higher absorption but still we do not approach the measured mirror QE for QT459B. Hence it has to be concluded that the mirror used for QT459B must have had a reflectivity much lower than the usual 95% for metallic mirrors. Indeed, when modelling the QE with a back surface reflectivity[2] of 0.3, which is the value for a *GaAs*-air interface, we are approaching the measured mirror QE to under 5%, the error for QE measurements on the experimental setup used.

In any case it has to be concluded that the substrate thickness must be reduced to virtually zero, removing the substrate right down to the active region if most of the light not absorbed in the first pass is to be reflected back towards the quantum wells. This could be most conveniently done for samples with an etch-stop next to the active region (see Chapter 5) but for some existing samples (especially *GaAs/InGaAs* ones) only lapping methods could be used which can reduce thickness to $50 - 80 \mu m$.

[1] $T_{sub} = T_{QW} \cdot (1 - A_{GaAs})^2$
[2] $T_{sub} = T_{QW} \cdot (1 - A_{GaAs}) \cdot R \cdot (1 - A_{GaAs})$

CHAPTER 4

Growth on patterned Substrates

4.1 Samples

4.1.1 Substrate Patterning

This section describes how a quantum well solar cell structure was grown on patterned substrates. The processing sequence for patterning is listed in detail in Table 4.1. Note the importance of the final O_2 plasma etch which ensures cleansing of the surface after a highly contaminating wet etching process. The etchant composition of the HF etch gives control on side wall angles to $\pm 5\%$ which is why we had to raise it to nominal 25° to make sure the sidewall angle wouldn't undercut $\alpha = 16°$.

A view of the resulting substrate is shown in Fig. 4.1 other parts can be seen in Figs. 4.2 & 4.3.

In this context it would be interesting to obtain results from a ray-tracing study into how the light-trapping efficiency varies with angle α to have a measure on the deterioration of the device performance due to etching uncertainties.

4.1.2 MBE Growth

Using one of the ICSTM Semiconductor IRC's solid source MBE machines and the growth sequence shown in Fig 4.4 U1113 is a cell grown at 630 $°C$ on patterned substrate, U1114 the control cell on a plane substrate and U1115 another control cell grown at 430 $°C$ to study the migration of the Beryllium p-dopant[1].

[1] this sample was not studied further as part of this work after some initial characterisation indicated that device quality had suffered from the low growth temperature

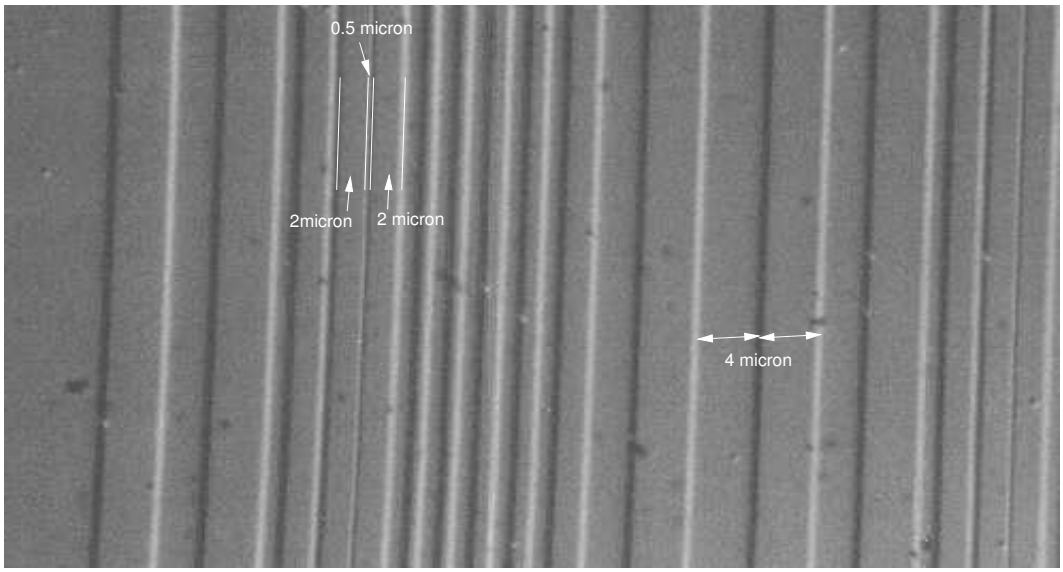

Fig. 4.1: SEM micrograph of grooves etched into substrate

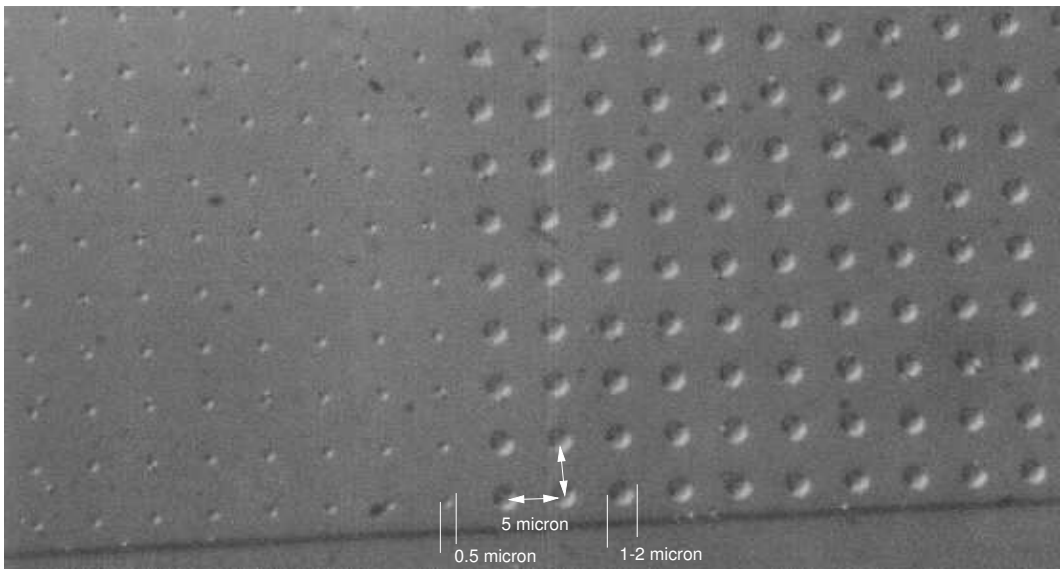

Fig. 4.2: SEM micrograph of cones etched into substrate

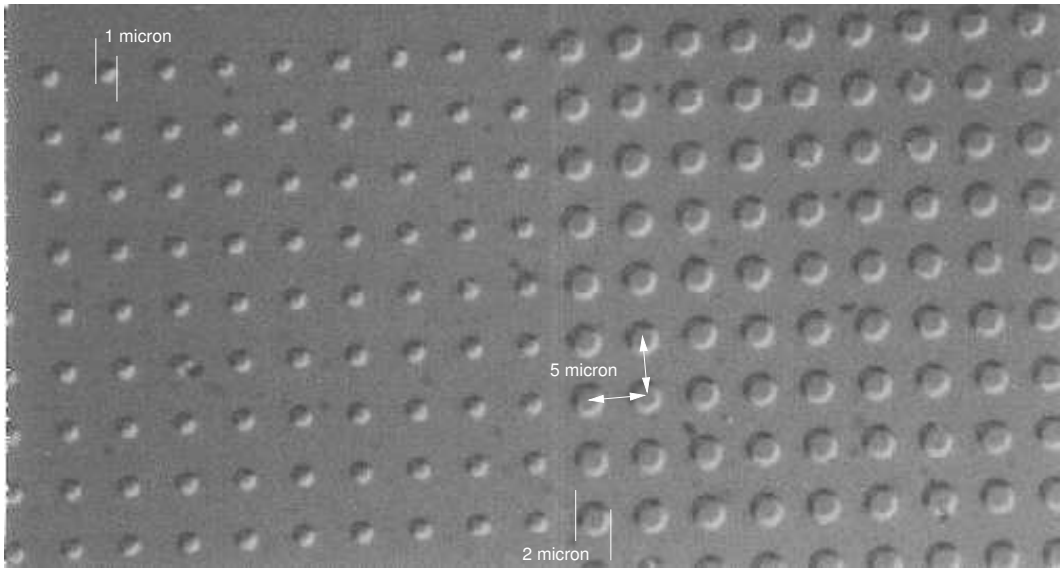

Fig. 4.3: SEM micrograph of mesas etched out of substrate

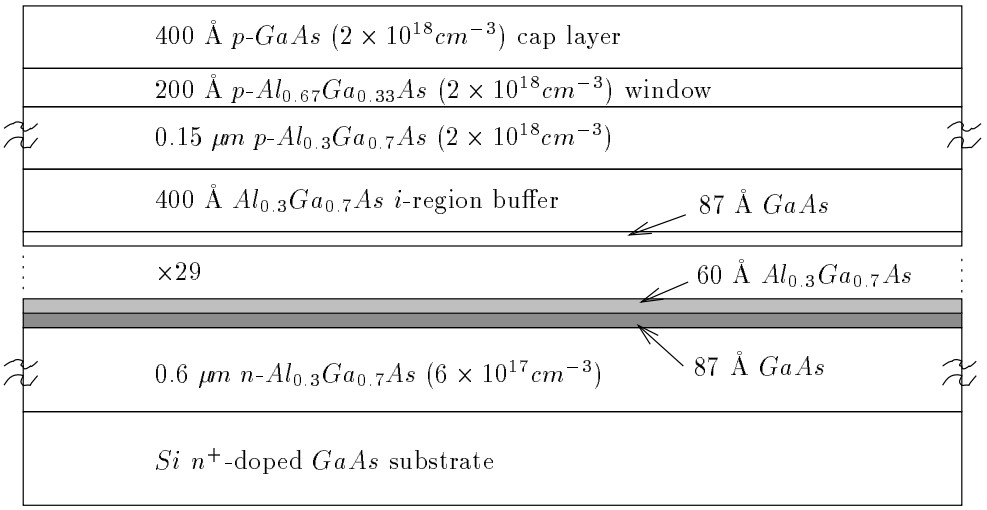

Fig. 4.4: U7113/4/5: 30 well MQW cells grown by MBE at 630 °C

Processing Step	**Variables**	**Comments**
1 hour 150°C Bake in Oven	1 hr	
15 mins Cool		
Microposit Primer 6500 rpm for **10** s	NO	
1805 Resist 5500 rpm for **30** s		
30 mins 90 °C Bake		
Cool		
Expose (0.6 s to 4 s)	0.5 s	
Develop **60** s		
Wash **1** min flowing DI water (state Ω)	18.2 M	
(30 s - 1 min) Oxygen Ash (state time)	**30** s	35 s ∼ 500 Å
30 s-1 min HCl:H_2O (1:4) (state time)	**30** s	
Wash in Flowing DI water for **30** s (state Ω)	18.2 M	
BHF:H_2O_2:H_2O (6:X:60) at T °C (state X, time and T)	6:3.8:60, 1 m 34 s, 10.4 °C	10.0 °C
Wash in Flowing DI for **2** mins (state Ω)	18.2 M	
Rinse in High Purity Acetone and then Propanal in ultra-sound Bath for **2** minute		
MP Stripper for **5** min in Ultrasonic Bath		
Wash in Flowing DI water for **1** min (state Ω)	18.2 M	
Microwave O_2 Plasma for **3** min O_2 ∼ 5 sccm, Power ∼ 30, Etch Rate 100nm/min		
1 min HCl:H_2O (1:4) then 1 min flowing DI water (state Ω)	18.2 M	
Calculated etch rate (Å/minute): 1275 Calculated etch time (minute-seconds): 1 min 34 sec Measured etch depth (Å): 2000±10 Measured facet angle(degree): ∼ 25° (nominal angle)		

Table 4.1: MCP Silicon doped substrate material WV 891/Si. Number 31, 2000Å etch with nominally 25° facet angle (Supplied to Christine Roberts for re-growth 18 April 1996)

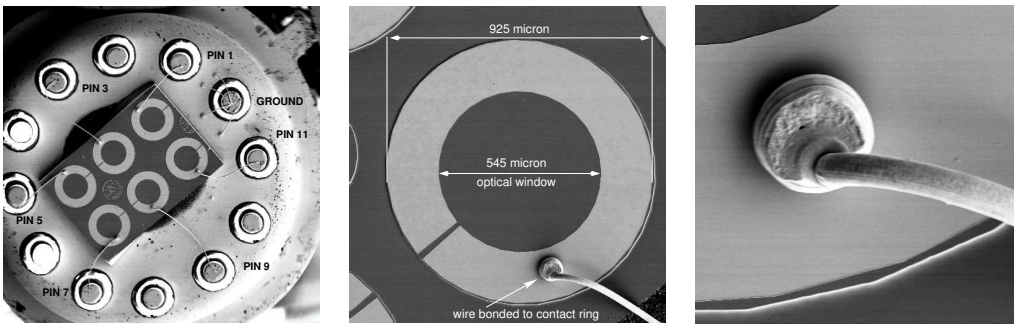

(a) Six devices mounted on a TO5 header

(b) Single device

(c) Wire bonded to contact ring

Fig. 4.5: SEM micrographs of TO5 headers

4.1.3 Processing and Mounting of Devices

The processing of the wafers grown consisted in partially covering them with AR-coating and defining devices on mesas using gold rings as contacts. Processed pieces of wafer were then mounted on TO5 headers shown in the SEI micrograph Fig. 4.5(a), Fig. 4.5(b) shows one cell blown up with size markers while Fig. 4.5(c) shows a contact wire bonded to the *Au* ring. The contact pins on the back of the headers are counted clockwise for reference, starting with 0 at the ground pin, which is notched (see Fig. 4.5(a)). The exact processing detail are specified in Table 4.2.

One of the main problems in making devices out of U7113 was to position the mask for mesa definition over patterned areas of the substrate, which is why the patterned devices each come on a header of their own (unlike Fig. 4.5 (a)) as they need individual processing. For easy reference devices defined on top of the patterned part of the U7113 wafer have a *p* appended to the device number, i.e. U7113p.

Some unpatterned U7113 & U7114 devices were also provided without AR-coating to study whether such processing has any detrimental effect on device quality.

4.2 Characterisation

I-V characteristics For characterisation current-voltage (I-V) characteristics were recorded using a source measurement unit, both in the dark and illuminated by a

Processing Step	**Variables**
Evaporate 50% $In-Ge$ alloy then Au all over back	**20** nm/**200** nm
Alloy back contact by ramping up temperature and subsequent cooling	**420**°C
Circular front contact with 600μm optical window defined in photo-resist, then lift off	
Evaporation of front contact, sequence: Au,Zn,Au	**5** nm, **10** nm, **200** nm
Alloying of front contact (take up to T, cool down)	**360**°C
Steps for AR-coated devices only	
Coating whole wafer with SiN_x in a silane-nitrogen plasma depositor (PECVD) at **300**°C	∼**100** nm/6.5 mins.
Cover wafer with photo-resist and expose over optical window for protection	
Remove unexposed resist and underlying AR coat using a Freon-Oxygen etch	**2** mins. @ RT
Following steps for both, AR and non-AR devices	
Definition of mesas using photo-lithography and using HB:acetic acid:potassium dichromate (1:1:1) in DI water (14.7 g/100 ml) to etch	**2** μm/**30** s
Cleaving and fixing devices to TO5 headers with epoxy for wire-bonding	

Table 4.2: Device processing and mounting at the EPSRC Central III-V Growth Facility in Sheffield as carried through by Malcolm A. Pate

Tungsten lamp. The dark I-V characteristics were used to establish the best devices on which light I-V and all subsequent measurements were performed.

Monochromatic I-V Fig. 4.6 shows how the optical setup discussed in Section 3.1 has been altered to allow measuring of monochromatic I-V and spectral response curves. The Lock-In amplification cancels out the dark current which is independent of the pulsed monochromatic light so that a monochromatic I-V curve measured across a 100 $k\Omega$ resistor shows values proportional to the photo-generated current I_{ph} and is related to the shift between dark and light I-V characteristic[2]

For a high quality solar cell I_{ph} should be constant over the whole bias range up to high forward biases, when the experiment breaks down as the diode resistance sinks below the 100 $k\Omega$ of the resistor across which the dark current is measured. Before that happens the depletion zone boundary (DZB) on either p- or n-side (depending

[2]note that monochromatic I-V measurements are still not fully understood and subject of ongoing research into the behaviour of quasi Fermi levels. For instance one cannot directly measure the generated current at constant bias as the latter will change due to the generated carriers

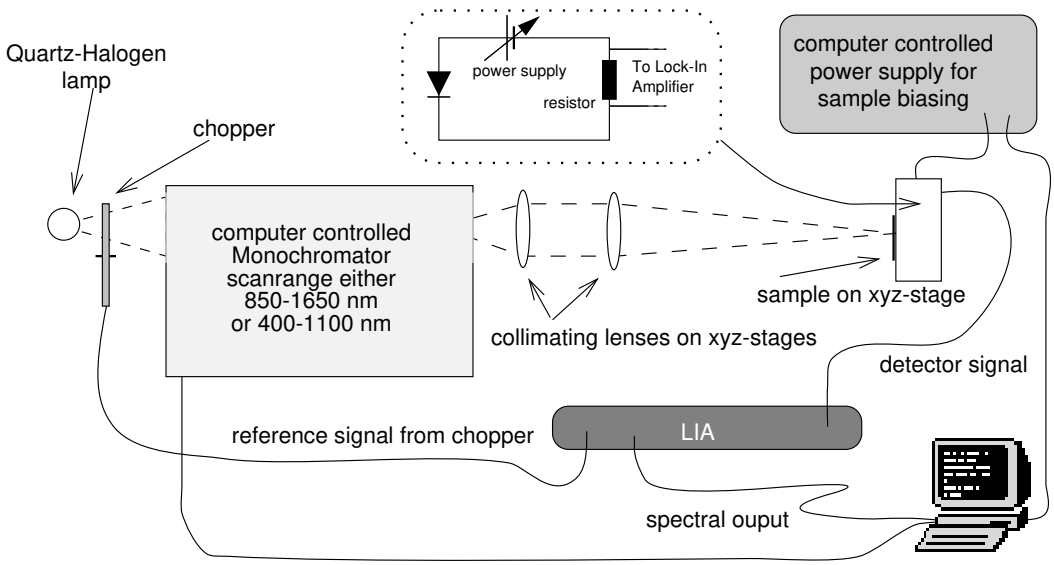

Fig. 4.6: Experimental setup altered for spectral response measurements

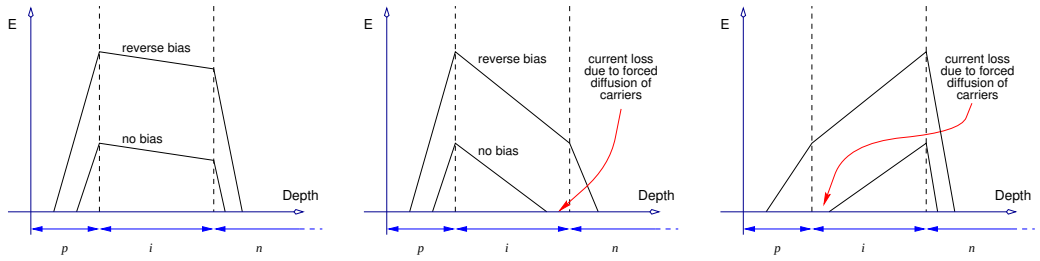

(a) Low level of background n-type doping

(b) High level of background n-type doping

(c) High level of background p-type doping

Fig. 4.7: Effects of i-region background doping on electric field

on the charge of the background doping) reaches the i-region of the cell at lower[3] biases (check Appendix A.2 for how the DZB changes with bias and see Fig. 4.7 (a)) so that carriers have to diffuse into the i-region to be accelerated by the junction field. Thus the current will decline until the DZB reaches into the i-region at a depth comparable to the the diffusion length, when a rapid plunge in the monochromatic I-V curves should occur. A monochromatic I-V of that type is shown in Fig. 4.8 for W405, a 30 well $AlGaAs/GaAs$ MQW solar cell.

For our samples one experiences a long gradual decay (c.f Fig. 4.8) as there seems to be a high level of background doping (usually around $10^{21}m^{-3}$) present in the i-region which causes the junction field to drop substantially across the i-region

[3] as the i-region must be wide to accommodate the wells

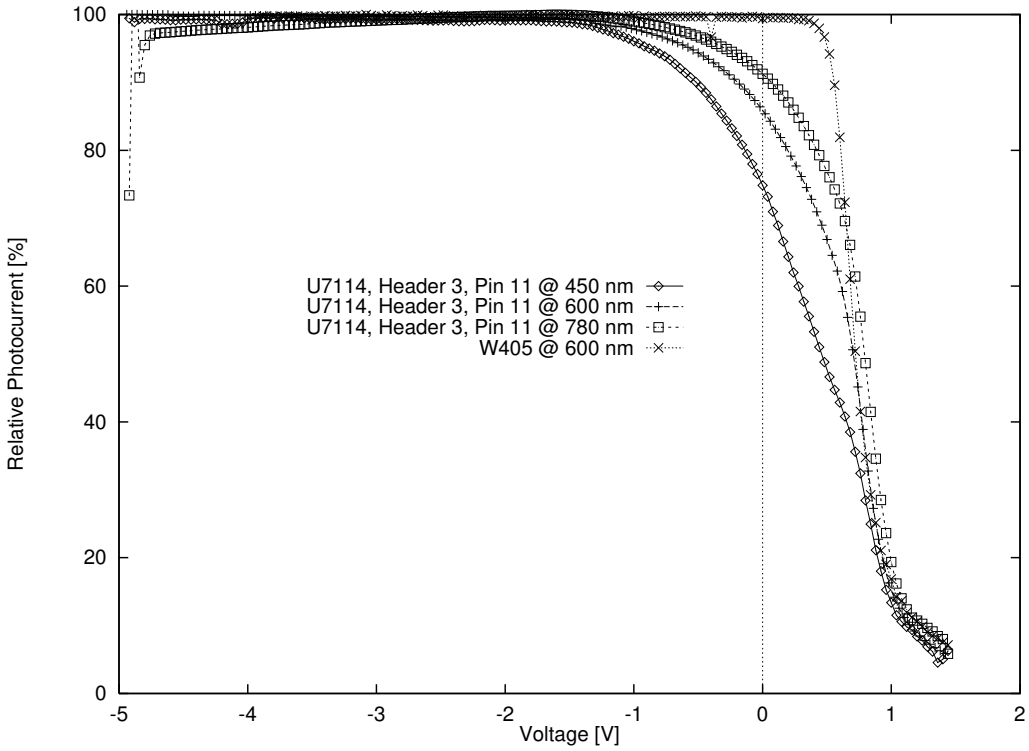

Fig. 4.8: Monochromatic I-V curves at different wavelengths

already. As one can see from comparison of Fig. 4.7 (a) with (b) & (c) the high background doping will cause the photo-generated current to trail off much earlier than for W405. This shows that there is a serious background doping problem with our wafers indeed.

For cells of low diode quality the monochromatic I-V current will not show constant behaviour even for reverse biases. Thus some devices exhibiting erratic behaviour from medium reverse biases onwards indicates early junction breakdown and therefore lower device quality.

All the monochromatic I-V curves were measured using a wavelength of 600 nm after it was checked via Fig. 4.8 how the monochromatic I-V curves change with wavelength: We can deduce that the bias at which the monochromatic I-V curve begins to show reasonably constant behaviour ($\sim -5\%$ below maximum) doesn't vary noticeably for the three wavelengths chosen. Thus choosing that bias (the bias should be as low as possible to avoid loss of features as demonstrated in Fig. 4.9 for the first two datasets) ensures the device is operating as a solar cell properly for

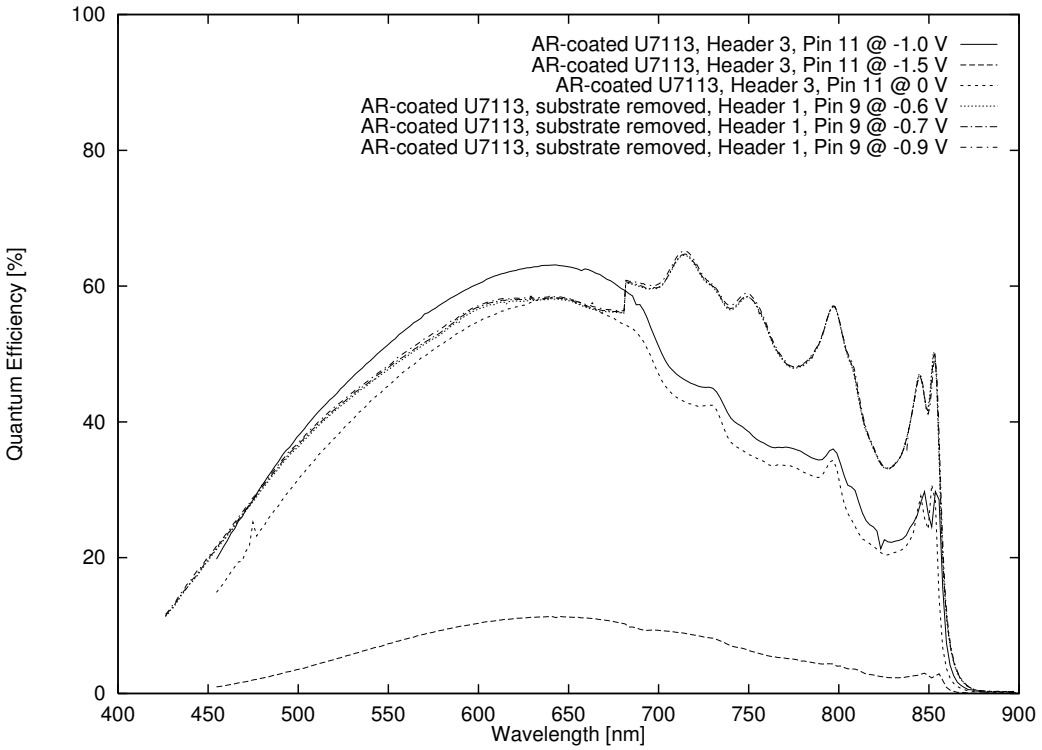

Fig. 4.9: Spectral response comparison for varying sample bias

measuring photo-generated current over a spectrum of $400 - 900\ nm$.

Ideally the spectral response is measured at zero bias with a flat monochromatic I-V beyond that point into forward bias. This was not possible for the devices measured as the monochromatic I-V trails off early which is a sure indication for high background doping. Thus the spectral response at zero bias is lower than for the bias chosen as explained above (see the first and third dataset in Fig. 4.9). To check the bias dependence Fig. 4.9 shows spectral response (SR) for one device at changing biases, one can clearly see that the SR doesn't vary noticeably for biases near the monochromatic I-V maximum (last three datasets[4]).

Spectral Response The same setup as for monochromatic I-V characteristics was used for recording spectral response spectra. This is done by measuring photo-current at the bias deduced from the monochromatic I-V measurements as explained before and relating this to the known spectral response of a Si photo-detector to eliminate optical lens aberrations, non-linearity of the grating etc. As explained

[4] the step near 700 nm is due to a glitch in the correction spectrum

in Section 1.2.2 spectral response (SR) curves show what percentage of incoming photons at energy $\hbar\omega$ are converted to an $e-h$ pair. This value naturally depends on the optical and electrical properties of a cell and its geometry and can rise over 100% for recycling of hot carriers.

Thus, by studying its spectral response we can see how well a solar cell converts light at given wavelengths. The low energy cutoff is due to the well bandgap (at 870 nm for $GaAs$ at room temperature[5]), below which no absorption is possible and for high energies the quantum efficiency is limited by recombination processes as photons of short wavelengths will be absorbed in the non-depleted part of the p-region in which the non-separated e-h-pairs can recombine non-radiatively. This is particularly true very close to the surface where interface states promote non-radiative recombination. At medium energies one can make out the $Al_{0.3}Ga_{0.7}As$ bandgap[6] at 690 nm where the SR dips down abruptly to the step-like[7] quantum well absorption with excitonic features just below the sub-band edges[8].

Optimisation To favour absorption in the i-region where carrier collection is far more efficient (see last paragraph), our p-layer was grown very thin (∼diffusion length[9]) and a window was incorporated to prevent photo-generated minority carriers from surface recombination. Such a window is usually $Al_{1-x}Ga_xAs$ of high aluminium fraction (typically 80%) and higher p-type doping than the surrounding material. The higher doping level pins the Fermi level to the valence band edge so that the higher gap is accommodated by an offset in the conduction band, acting as a deflector for minority electrons (c.f. Fig. 1.2). Another optimising feature could be a graded p-region which leads to a built-in field for carrier separation and hence to better carrier collection at short wavelengths. Another possible approach is to grow the window directly adjacent to the i-region resulting in a heterojunction

[5] $E_{gap}(GaAs) = 1.519eV - \frac{5.405\cdot10^{-4}T^2}{204+T}eV$ for T in Kelvin (Ref. [Sze, 1981])
[6] empirical relation: $E_{gap}(Al_xGa_{1-x}As) = E_{gap}(GaAs) + 1.247 \cdot x$
[7] due to the step-like 2 dimensional density of states
[8] at (sub-band energy offset - exciton binding energy)
[9] which for $AlGaAs$ is very short for reasons explained later

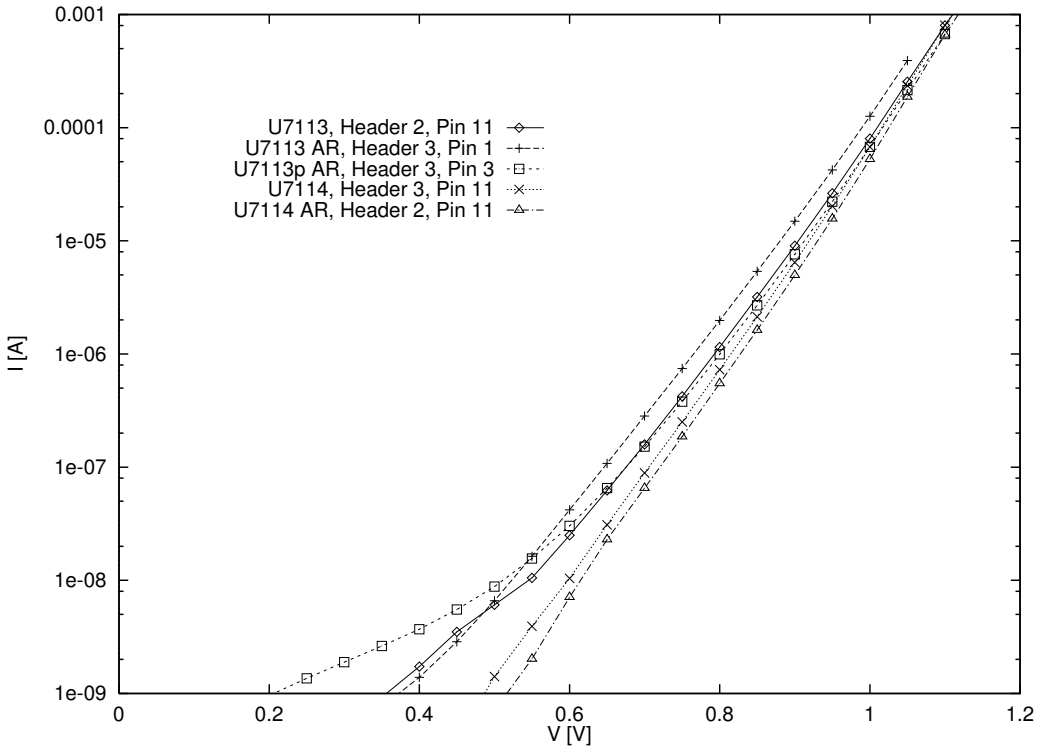

Fig. 4.10: Dark I-V comparison for five different sample types

cell. Intermediate wavelengths are absorbed in the space charge region so for better spectral response at higher wavelengths extending the *i*-region to a maximum is a design rule, limited by the fact that the junction field cannot be maintained across very thick *i*-regions.

It's also very important to have a look at the reflective properties of devices as this is the main optical limitation which cannot be easily overcome — standard anti-reflection (AR) coatings are rather wavelength specific due to their $\lambda/4$ thickness for which the Airy calculation shows a minimum in reflectivity for that specific wavelength λ.

4.3 Results with Substrate remaining

When studying the measured data no enhancement in current densities or spectral response could be seen as the substrate had not been etched away yet, so there's no *AlGaAs*-air interface at the back to give rise to total internal reflection.

What we can say though, is that despite displaying some deterioration compared

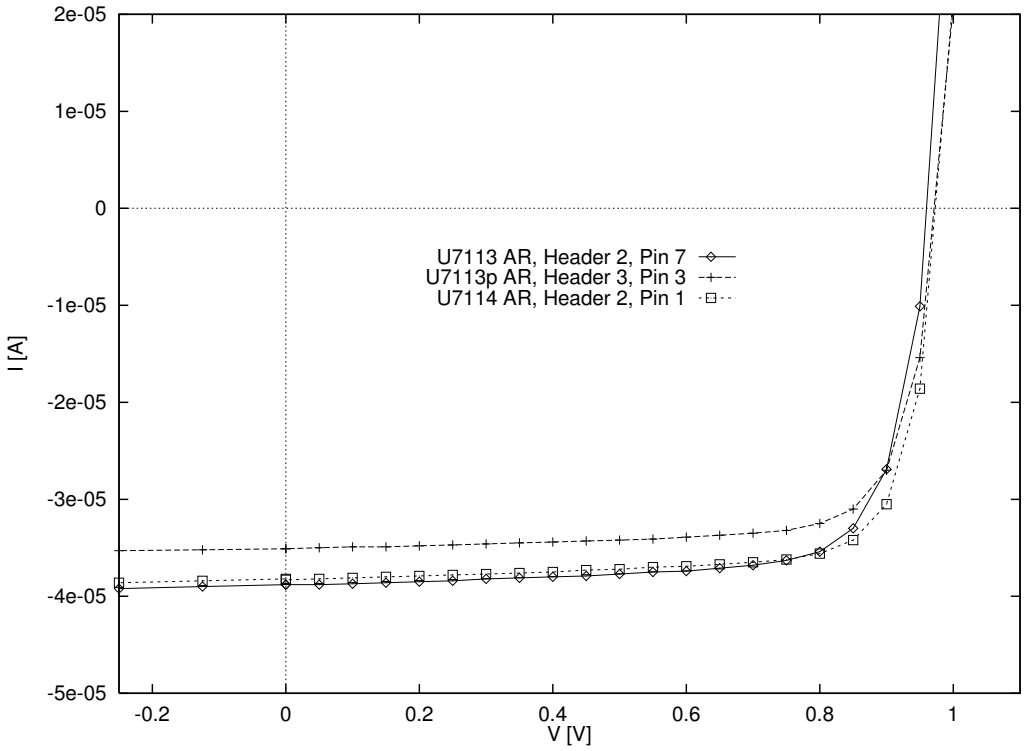

Fig. 4.11: Light I-V comparison for three AR-coated sample types

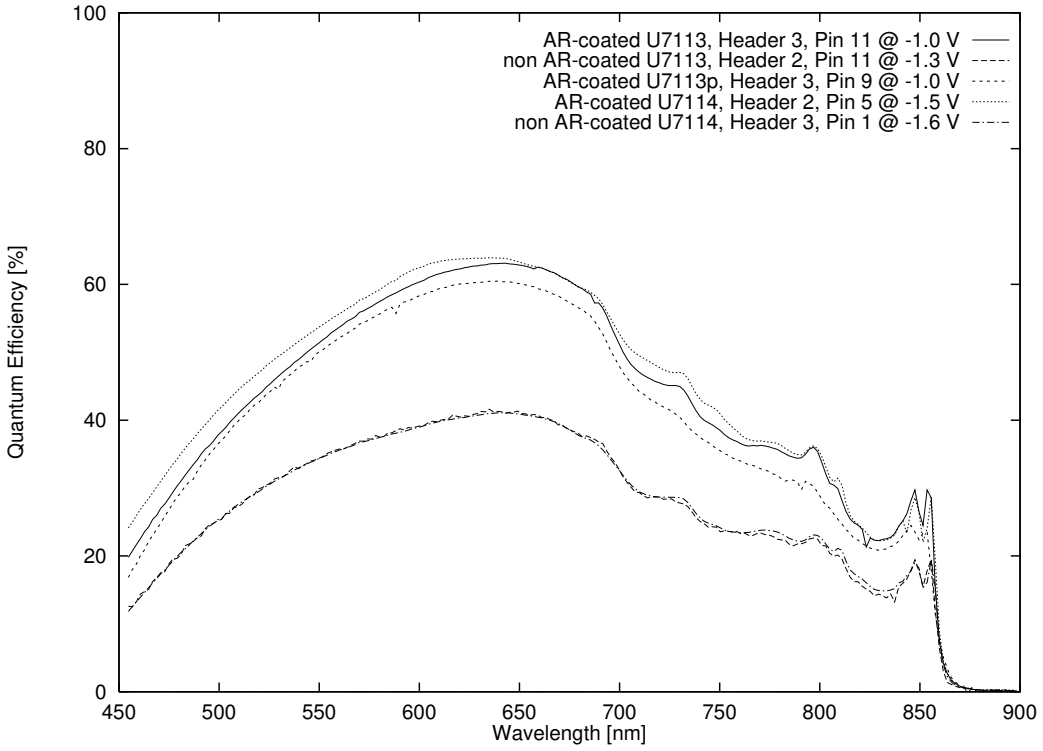

Fig. 4.12: Comparison of spectral responses for five different sample types

to the control the material grown on top of the patterned part of the substrate still fulfils the requirements for good solar cell material: The dark I-V curves show reasonable diode behaviour (Fig. 4.10 — note there seems to be no change in diode quality due to AR processing), the light I-V's show photo-voltaic conversion very much like the control (Fig. 4.11) and, most importantly, the spectral response (Fig. 4.12) does not seem to have suffered considerably from the patterned substrate either. The slightly lower SR of the patterned U7113p device might indicate a slight detrimental effect on device quality when using heavily processed patterned substrate which is likely to introduce impurities even after undergoing plasma cleaning (c.f. Section 4.1.1). The non-AR devices have been included in the SR plot to demonstrate the importance of anti-reflective properties of the solar cell surface.

The reason the spectral response does not reach the levels above 80% as seen for instance in Si though, is that $Al_{1-x}Ga_xAs$ is such a bad solar cell material in terms of minority carrier lifetime. Because of that a high percentage of carriers recombine non-radiatively at the abundant impurities present before collection at the external contacts is possible. This could be remedied by changing to lattice matched $Ga_{0.52}In_{0.48}P$ or completely different material systems like $InP/InGaAs$ (which unfortunately has it's own material problems with Zn dopant diffusion).

4.4 Results following Substrate Removal

Due to the tight time-scale for this project, it was decided that the final processing step of etching off the substrate would only be carried out on U7113 with the unpatterned parts acting as control for the patterned substrate devices. As I-V-characterisation suggests U7113 device quality to be slightly inferior to the U7114 series[10], this is the only way to achieve comparable patterned and control cells !

When the devices were processed and mounted on TO5 headers using epoxy for fixture again, some of them had a gold mirror evaporated on their back to check whether the samples without it actually do exhibit total reflection. The dark I-V-

[10] presumably due to the additional processing during patterning

measurements Fig. 4.13 looked promising as they compare well with the very similar values in Fig. 4.10 and indeed enhancements in the light I-V curves can be seen (Fig. 4.14) when comparing the four new device types to the old ones with substrate.

One peculiarity about the light I-V characteristics is that the gold mirrored U7113p devices exhibited very low open circuit current, two of them just around 20 μA, while one would expect them to outperform the best I-V characteristics as displayed by the non-mirrored U7113p ones. It might well be that those four devices (which behave very differently) have been made of a particularly bad part of the patterned wafer but to be sure of that a full investigation using SEM, SIMS and other methods would have to be carried through. As regards the question why there should be any problem at all with some of the devices, it was mentioned before that the monochromatic I-V shape suggests severe background doping problems. These haven't occurred for previous runs on that MBE machine at the IRC but after technical problems with the *Al* source dopant impurities might have been introduced. Another possible explanation for such device behaviour could be dopant diffusion into the *i*-region, which could be checked on using SIMS.

The result shown in Fig. 4.15 shows a comparison of the four new device types and also the three ones with substrate to demonstrate the enhancement: The unpatterned devices' spectral response is surprisingly similar to the patterned ones and the gold mirror shows little difference to the epoxy case. Nevertheless we can see quite a substantial enhancement over the spectral response before removing the substrate shown in the first three datasets. There definitely is a strong mirroring effect present in all samples with removed substrate, even the epoxy ones, as indicated by the prominent Fabry-Perot features on top the low energy part of the spectrum.

Such features show that the top and back surface must be very plane-parallel for the interference condition to be fulfilled in such a strong manner. Actually one would not expect this behaviour from the patterned substrate samples but when one takes a look at the pattern (e.g. Fig. 4.1) it's quite obvious a high percentage of the area is actually plane. This observation is supported by the fact that the

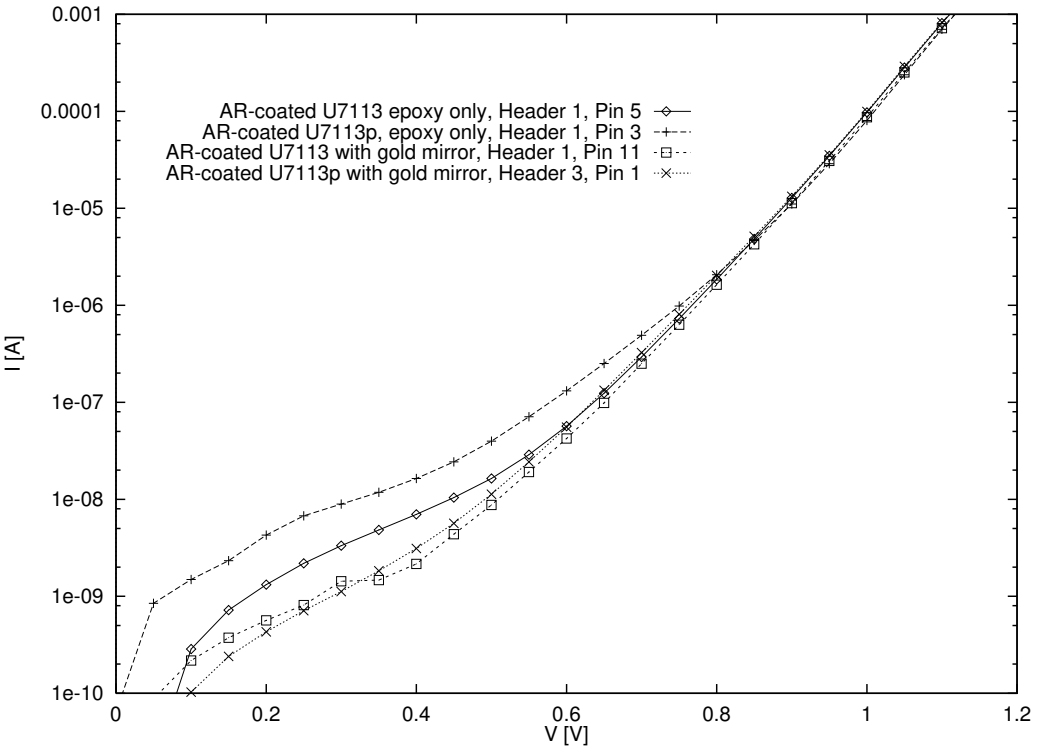

Fig. 4.13: Dark I-V comparison for the four non-substrate sample types

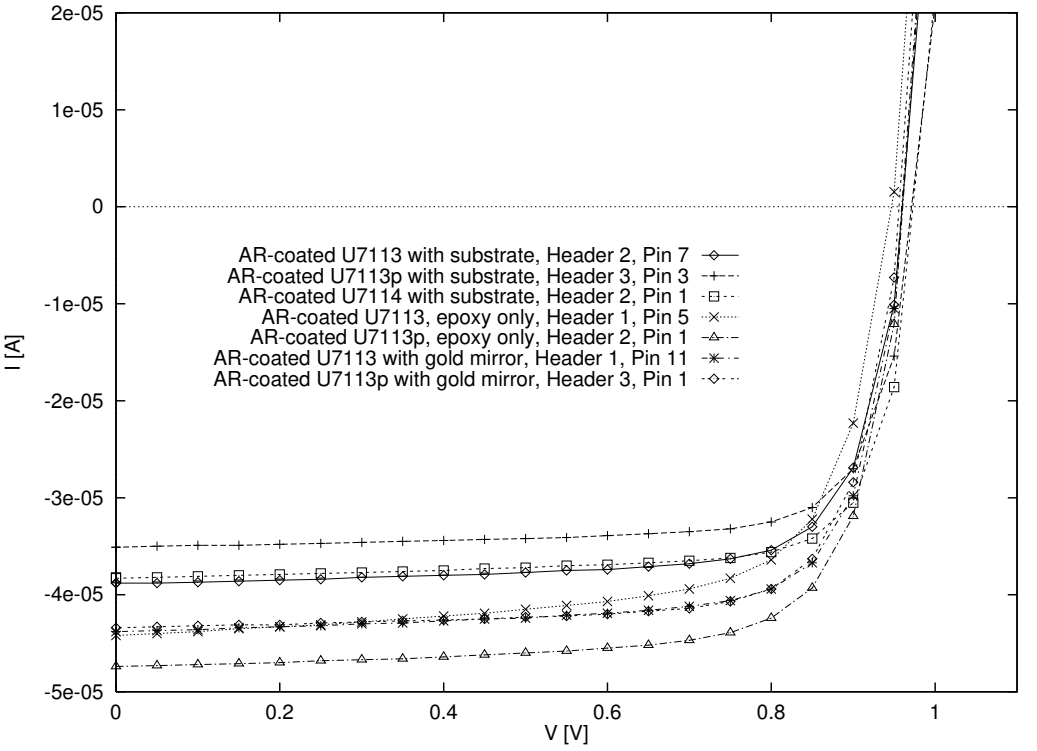

Fig. 4.14: Light I-V comparison for all seven AR-coated sample types

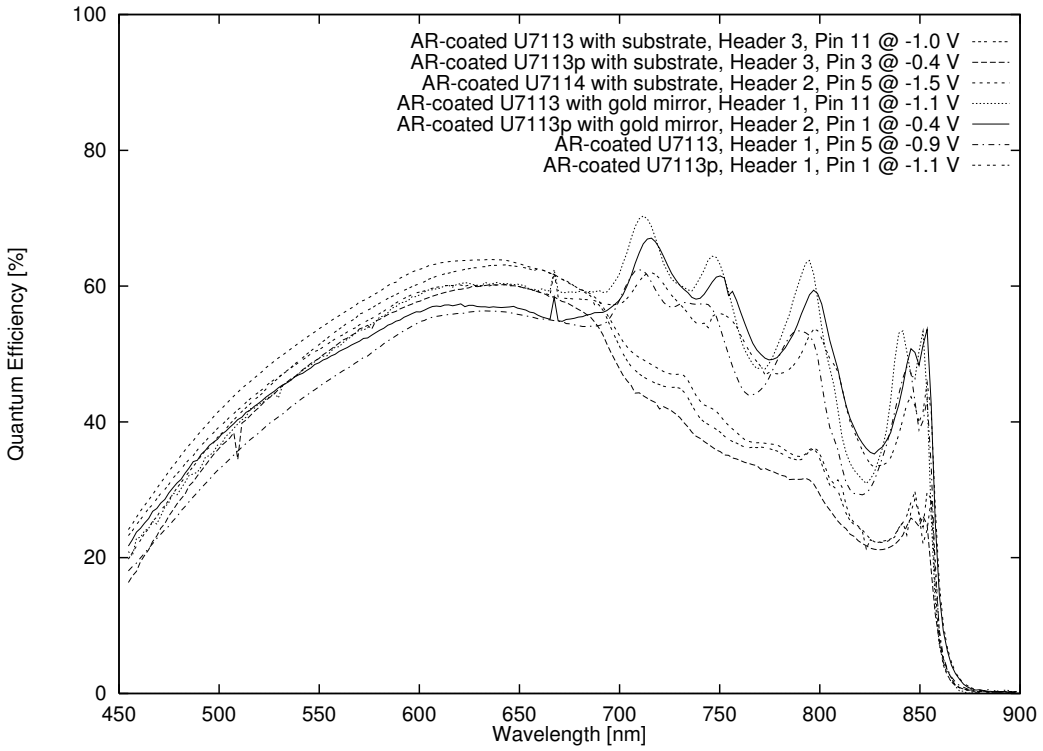

Fig. 4.15: Spectral Response comparison for all seven AR-coated sample types

Fabry-Perot oscillations exhibit slightly lower amplitude for the patterned samples as the low percentage of light beams which hits the inclined parts of the back surface will not take part in the Fabry-Perot interference. This could be understood as an indirect indication for light trapping actually occurring in the patterned samples.

As there is no total reflection for a horizontal $AlGaAs$-air interface at the back, the samples with additional gold mirror should perform much better which is actually not the case - for some reason the spectral response of the devices without mirror (epoxy only) can keep up with the gold ones. This is rather intriguing as epoxy has comparable refractive index ($\sim$1.5) to air and does not exhibit plasma reflection like a metal so one would not expect higher reflectivity than 0.3 for the back surface. Nevertheless the Fabry-Perot oscillations can be seen just as clearly as for the 95% reflective gold mirror.

The conclusion to arrive at is that the TCRC mask sets used for patterning quantum dots are not suitable for producing light trapping structures for QWSC solar cells due to the too large feature spacing. To carry on this work a new mask

set would have to be designed and written by e-beam lithography at TCRC which produces cones and ridges of closer spacing which is apparently possible as can be seen in the middle part of Fig. 4.1. Nevertheless the samples produced so far show potential - simply from the second pass of light through the wells for plane mirrors we have achieved quite impressive enhancements in efficiency as it is summed up in Table 4.3.

Even with the absence of prominent light trapping we can also see quite a substantial enhancement over the spectral response before removing the substrate just by enabling the two-pass mirroring. It is particularly interesting to have a closer look at the actual SR in the QW region where the highest enhancement is to be expected from the doubled path-length of light due to the low QW absorption: The enhancement is indeed more pronounced below $AlGaAs$ bandgap, as it would be expected when considering that the bulk absorption approaches 100% while the quantum well absorption is low (1% per allowed transition and well as a rule of thumb). In particular the excitonic features below the lowest quantised well energy level around 850 nm show about two fold SR enhancement but this continues right up to the $AlGaAs$ bandgap near 700 nm. Such good resolution of excitons at room temperature is also an indication for very high well quality which signifies perfect overgrowth on top of the featured substrate (see Section 4.5).

Thus it was rather impressively shown that mirroring yields the anticipated efficiency enhancement for the quantum wells in the case of reduced substrate absorption. It can also be said that in the production of these cells a high level of perfection in countering processing induced defects and impurities has already been attained as the good spectral response features indicate although the comparison with U7114 shows there is still room left for improvement. Comparing patterned and unpatterned case one could even go further and say that the slight effect of minimal light trapping has been indirectly documented by the lower Fabry-Perot amplitudes. Alas, this cannot be ascertained for sure using a setup with $\pm$5% error for the SR spectra until samples produced with the abovementioned adapted mask

before substrate removal					
Sample		u7113	u7113p	u7114	
Devices type		AR coated	AR-coated, patterned	AR-coated	
Intensity		1e+03	1e+03	1e+03	W/m^2
P_{in}		0.00023	0.00023	0.00023	W
Area		2.3e-07	2.3e-07	2.3e-07	m^2
V_{oc}		0.98	1.02	1.03	V
I_{sc}		-3.88e-05	-3.51e-05	-3.83e-05	A
P_{max}		2.73e-05	2.61e-05	2.86e-05	W
V_{max}		0.819	0.831	0.84	V
I_{max}		-3.46e-05	-3.17e-05	-3.46e-05	A
FF		0.718	0.732	0.725	
Efficiency		11.9	11.4	12.4	%
Temperature		23.1	22.9	23.2	°C

after substrate removal					
Sample	u7113	u7113	u7113p	u7113p	
Device type	AR-coated, epoxy only	AR-coated, gold mirror	AR-coated, patterned, epoxy only	AR-coated, patterned, gold mirror	
Intensity	1e+03	1e+03	1e+03	1e+03	W/m^2
P_{in}	0.000233	0.000233	0.000233	0.000233	W
Area	2.33e-07	2.33e-07	2.33e-07	2.33e-07	m^2
V_{oc}	1.01	0.977	0.981	0.967	V
I_{sc}	-4.42e-05	-4.38e-05	-4.74e-05	-4.34e-05	A
P_{max}	2.88e-05	3.05e-05	3.3e-05	3.06e-05	W
V_{max}	0.784	0.816	0.811	0.808	V
I_{max}	-3.71e-05	-3.86e-05	-4.18e-05	-3.9e-05	A
FF	0.644	0.712	0.709	0.729	
Efficiency	12.4	13.1	14.1	13.1	%
Temperature	26.6	27	26.9	27.1	°C

Table 4.3: Comparison of efficiencies for all seven AR-coated sample types

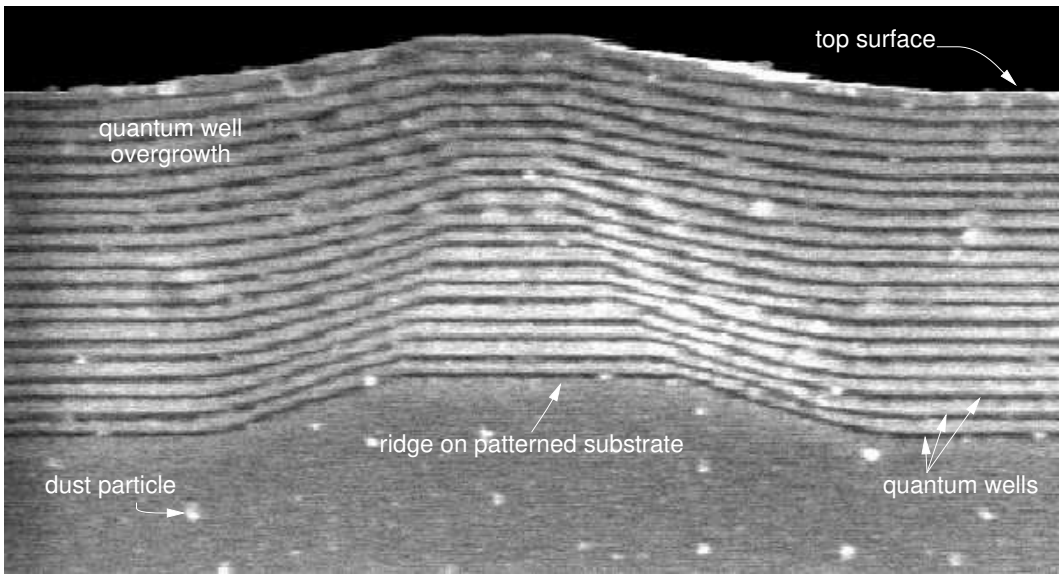

Fig. 4.16: Overgrowth on patterned substrate (dark lines are quantum wells)

set become available which should exhibit a complete lack of Fabry-Perot features in favour of higher efficiencies due to multiple path length enhancement.

4.5 Characterisation of Overgrowth

In parallel, part of the U7113 wafer was sent to TCRC for cross-sectional SEM studies of the overgrowth on the pattern to help identify whether imperfections have been introduced which degrade solar cell performance. Fig. 4.16 does not suggest this is the case as the quantum wells can be clearly seen to follow the pattern in an undisrupted way. The micrograph is one of TCRC's own overgrowth studies as crossectional SEM would have involved lengthy destructive sample preparation which couldn't be accomplished in time. Nevertheless good overgrowth for our own samples has been suggested by the presence of excitonic features in the SR as it was discussed in the preceding section.

CHAPTER 5

Patterning of MQW Solar Cell Material

In Chapter 4 we have pursued the approach to light trapping involving MBE growth on top of a substrate patterned by anisotropic etching. To achieve light trapping properties the substrate had to be etched down to the pattern so total reflection at the $GaAs$-air interface occurs. Now imagine the patterning step shifted to the end of a production sequence. In this way it is possible to upgrade a ready-grown cell to a light trapping structure by etching patterns into the substrate on its back. Remembering the results of Chapter 3 it is crucial to reduce the substrate first to reduce absorptive losses in it before commencing patterning.

5.1 Eliminating Substrate Absorption

Some of the group's best solar cell material, namely QT459B, a $GaAs/InGaAs$ cell, was processed at the EPSRC III-V Growth Facility with the aim to reduce the wafer substrate to 2–3 μm. The resulting brittleness of the 5 μm thin wafer pieces made handling extremely difficult.

A rather brilliant solution for this problem was the use of dental floss ! Heating the wax around the string established good contact to the brittle wafers for careful transfer from the etching bath to glass slides. Molten wax was used again to keep the wafers fixed on the slides. These slides were then sent to Toshiba Cambridge Research Centre for SEM study using their cathodoluminescence (CL) stage and patterning:

Due to the sample brittleness contact printing cannot possibly be used for transfer of the mask pattern. Thus it was decided a newly installed electron beam lithog-

raphy setup would be used for writing the mask pattern into *e*-beam resist covering the samples.

5.2 Patterning and Device Fabrication

Before commencing patterning it was deemed important to take a look at the surface morphology of the thin wafer pieces first, as planar isotropy is crucial for obtaining regular patterns of the required sidewall angle by anisotropic etching. This proved to be impossible for a long time due to technical problems with the wet pumping system on the Oxford Instruments CL stage used on the Hitachi SEM at TCRC.

Additionally the thin wafer pieces being mounted on glass added the complication that charge buildup is to be expected when trying to image them in the SEM. A possible solution for that problem would be evaporation of a thin metal layer on top of the wafers to offer the impinging electrons an opportunity to flow off to ground. This hasn't been tried before at TCRC so that some preparatory testing would have to be carried through first which time would not permit.

When taking into account that vertical resolution is comparatively low for SEM's depending on the depth of field (resulting in a tradeoff between high vertical and high horizontal resolution) the only way to obtain authoritative answers on surface roughness is by cross-sectional SEM anyway. But this method involving slicing the wafer parallel to the surface would hardly be applicable to the thin samples at hand for reasons of handling and above all it's destructive. After finished patterning one then has to expect problems with the final stage of mounting the even thinner patterned wafer pieces on T05 device headers.

Thus TCRC provided the CL micrograph Fig. 5.1 instead which shows a reasonably smooth surface of U7113 in cross-section. The magnification used was 30 000× with a beam energy of 5keV. A stain etch (H_2O_2:NH_4OH:H_2O at ratio 19:1:200 for 10 seconds) selectively etched the GaAs in the structure to give a better contrast with the $AlGaAs$ in the cross-section of the structure. The micrograph gives rise to

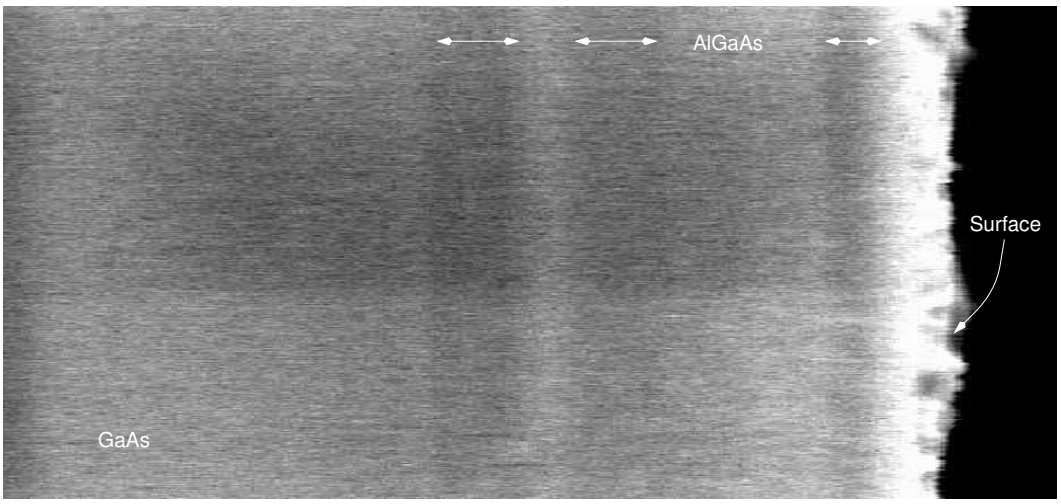

Fig. 5.1: Cross-sectional SEM micrograph of U7113 wafer

the hope that a surface flat enough for patterning might be expected for the thinned down wafers as well. With the deadline for submission of this thesis too close it was in the end not possible to move on to the actual processing stage.

One comes to the conclusion that this approach to achieving light-trapping in QW solar cells is problem-ridden but with the skill displayed by the processors so far it's likely to succeed[1]. Inadvertently this will take some more time which has the unfortunate consequence that light trapping could not be studied for devices in existence in this thesis.

[1] although final microscope studies of the glass slides actually revealed that one of the two wafers had fallen into pieces completely

CHAPTER 6

Conclusions

The flowchart Fig. 6.1 shows the progress made in this project, the detailed summary follows:

1. In Chapter 2 geometrical light trapping in a solar cell was investigated based on transversal reflection from patterned back surfaces leading to internal total reflection from a flat top. As a result the optimum angle of inclination for mesas or grooves at the rear of a solar cell with a plane top was identified as 16°. The average optical path-length enhancement exceeds the factor 4. To determine the actual path-length enhancement a ray tracing analysis, for instance using the UNSW package *Raymond*, should be carried out on the structures of interest. Clearly patterns with different slopes for adjacent reflective faces could promote such an average enhancement further by eliminating the possibility of direct reflection out of the cell structure.

2. The measurements in the next chapter (Chapter 3) showed that absorptive processes in doped $GaAs$ substrate will inhibit light trapping when using mirroring or patterning on the back of thick substrate on which a cell was grown.

   The approach of modelling this absorption as pure free-carrier absorption showed that a second absorptive process must be present as suggested by the spectral shape of the measured absorption spectrum for n-$GaAs$. This process is most likely to be attributed to inter-valley scattering which still needs to be incorporated into a complete theoretical model for substrate absorption. In an attempt to emulate such a model the measured $GaAs$ absorption was used instead of mere free-carrier absorption which gives a better estimate of the enhancement in the quantum well region's spectral response to expect.

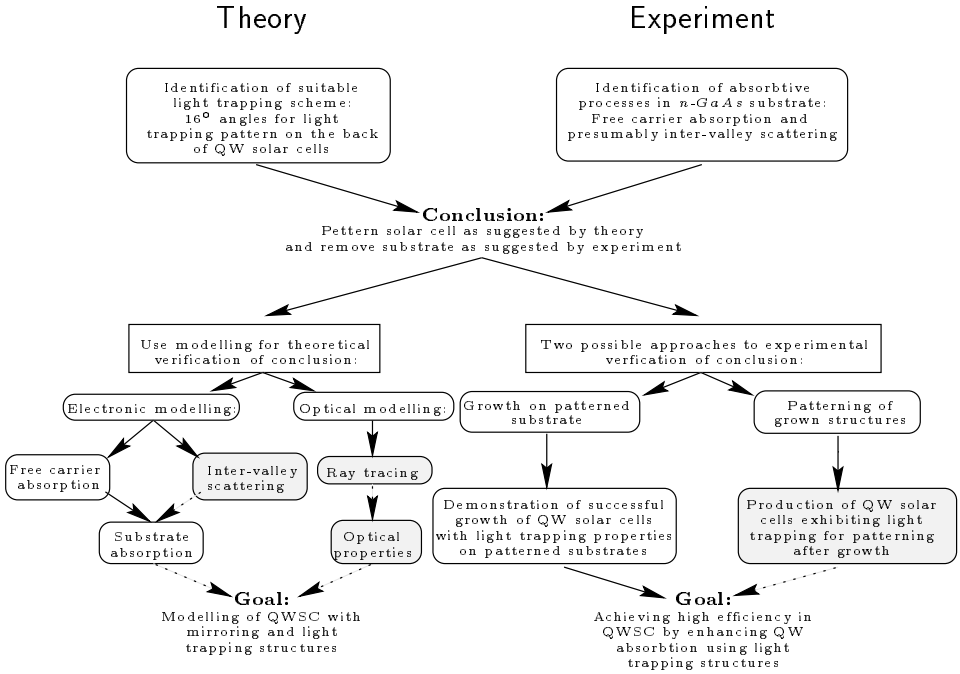

Fig. 6.1: Progress flowchart for this M. Sc. project — the shaded activities could not been concluded as explained in the thesis

On the question of the maximum thickness tolerable for light-trapping the conclusion was that as much substrate as possible has to be removed via etching or mechanical methods. This leads to two approaches resulting in minimum substrate thickness.

3. In Chapter 4 it was discussed how a cell can be grown by solid source MBE on top of a patterned substrate, which is subsequently etched down to reveal the pattern. The most prominent result was to prove that undisrupted QW overgrowth on top of patterned substrate is possible and shows little deterioration in material quality compared to control devices on unpatterned parts of the same wafer. The spectral response of the devices exhibits prominent Fabry-Perot oscillations which suggests very plane-parallel top and back surfaces, while a loss in oscillation amplitude for patterned devices might indicate a possible light trapping effect in comparison to the controls.

The conclusion to arrive at is that the spacing of the pattern is too large for the samples to exhibit light trapping as anticipated. Thus a new mask set with a pattern resulting in less plane area has to be designed for future measurements.

A very puzzling question remains how a Fabry-Perot cavity has been established for the cells without the gold rear mirror but supposedly a plain $AlGaAs$-epoxy interface at the back. Clearly investigations into the properties of the evaporated Au mirror have to be conducted as well, particularly when taking into account that modelling carried out in Chapter 3 suggested possible problems with evporated mirrors. Also high background doping in the i-regions has been encountered which indicates problems with the Al-source of the MBE machine used might have given rise to a source of dopant impurities.

In any case a substantial enhancement in spectral response from the quantum well region and efficiency has been achieved using plain mirroring already.

4. A second method for producing a solar cell exhibiting light-trapping consisted in thinning down the substrate of an existing cell and defining the pattern subsequently. This has been described in Chapter 5.

   It was demonstrated using cross-sectional SEM micrographs how a cell thinned down by an etchant exhibits a surface flat enough for subsequent patterning using the anisotropic etching technique employed at TCRC. It still has to be seen though whether these very brittle wafers can withstand the potential hazards during preparation and mounting which is paramount for experimental verification of light-trapping using control cells.

CHAPTER 7

Acknowledgements

First I'd like to thank all my collaborators for providing me with the means for carrying my work through: Stuart Holmes at the Toshiba Research Laboratory in Cambridge for contributing with his expertise in patterning substrates and his interest in this work, Malcolm Pate at the EPSRC Central III-V Semiconductor Facility in Sheffield for his excellent processing and Christine Roberts at the Semiconductor Interdisciplinary Research Centre, ICSTM for growth of U7113-5.

Also I feel very obligated to Keith Barnham, who made this thesis possible by supervising it and was very helpful with regard to my admission to this M. Sc. course in the first place, and all the brilliant researches in his Quantum Well Solar Cell Group for their help and encouragement: Ian Ballard (nice SEM pictures, aren't they ? Ever since A20 you have been very helpful, I really appreciated that !), Jenny Barnes (thanks for having such immeasurable patience with me.), James 'Models'r'Us' Connolly (you are brilliant enough to find a job even with your Fortran knowledge impeding you !), Paul Griffin (the Sheffield conduit), Enrique Gruenbaum (who gave me a very interesting account of his life), Jenny Nelson (thanks for all the coffee, your proofreading and patiently answering all my questions.) & Alex Zachariou (the clarinet playing InP specialist in despair of people pronouncing his name funnily)

Special thanks go to the LaTeX3 project and the authors of gnufit, xfig, xmgr & xv. Without these amazingly powerful freeware packages this thesis would have never been written.

Finally I'll forever be very grateful to all the people who made my M. Sc. year at IC in London possible and worthwhile. You know who you are.

THANK YOU !

APPENDIX **A**

p-n Junctions

A.1 Intrinsic Semiconductors

To obtain carrier densities for a semi-conducting material we integrate the density of states $g(E)$ weighted with the statistical Fermi-Dirac carrier distribution $f(E)$ over all energies in valence and conduction band respectively:

$$\begin{aligned} n_{cb}(T) &= \int_{E_C}^{\infty} g_{cb}(E) f(E) dE \\ p_{vb}(T) &= \int_{\infty}^{E_V} g_{vb}(E)(1 - f(E)) dE \end{aligned}$$

We employ the classical approximation of $f(E) = (\exp(\frac{E-E_F}{KT}) + 1)^{-1}$ by Boltzmann statistics[1]:

$$f(E) \longmapsto e^{\frac{E-E_F}{KT}} \text{and} (1 - f(E)) \longmapsto e^{-\frac{E_F-E}{KT}}$$

As $g_{cb} = \frac{1}{2\pi h^3}(2m_e^*)^{3/2}(E - E_C)^{1/2}$, $g_{vb} = \frac{1}{2\pi h^3}(2m_h^*)^{3/2}(E_V - E)^{1/2}$ solving the integrals concludes in

$$\begin{aligned} n_{cb} &= \overbrace{2h^{-3}(2\pi m_e^* K_B T)^{3/2}}^{N_{cb}} \cdot e^{-\frac{E_C-E_F}{KT}} \\ p_{vb} &= \underbrace{2h^{-3}(2\pi m_h^* K_B T)^{3/2}}_{N_{vb}} \cdot e^{-\frac{E_F-E_V}{KT}} \end{aligned}$$

which results in the Law of Mass Action:

$$n \cdot p \doteq n_i^2 \Rightarrow n_i = 2h^{-3}(2\pi K_B T)^{3/2}(m_h^* m_e^*)^{3/4} \cdot e^{-\frac{E_{Gap}}{2KT}}$$

A.2 The Poisson Equation at the p-n Interface

For understanding how the depletion zone around a p-n junction forms we'll have a look at what happens after p and n-type material have been brought into contact:

[1] $E_C - E_F \gg KT$, $E_F - E_V \gg KT$ i.e. the Fermi energy is in the bandgap, well away from the band edges

After the p-n semiconductor contact at $x = 0$ has been established, valence band electrons flood from the n-region into into the p-region and leave un- compensated donors in a zone of approximate depth x_n behind, accordingly the holes in the conduction band flow from p to n-side of the junction, leaving acceptors behind in a zone of approximate depth x_p:

$$\rho_{sc} = \begin{cases} eN_D & \text{for} \quad 0 < x < x_n \\ -eN_a & \text{for} \quad -x_p < x < 0 \end{cases}$$

This charge density gives rise to an electric field of triangular shape for $-x_p < x < x_n$ which can be calculated using Poisson's Equation:

$$\begin{aligned} \vec{\nabla}\vec{E} &= \frac{\rho_{sc}}{\epsilon_{sc}\epsilon_0} \\ \Rightarrow E(x) &= \begin{cases} \frac{eN_D}{\epsilon_0\epsilon_{sc}}(x - x_n) & \text{for} \quad 0 < x < x_n \\ \frac{-eN_A}{\epsilon_0\epsilon_{sc}}(x + x_p) & \text{for} \quad -x_p < x < 0 \end{cases} \end{aligned}$$

We can see that the maximum field at $x = 0$ is given by $E_{max} = \frac{eN_d x_n}{\epsilon_0\epsilon_{sc}} = \frac{eN_a x_p}{\epsilon_0\epsilon_{sc}}$. The resulting potential ψ for $-x_p < x < x_n$ is given by $\vec{E} = -\vec{\nabla}\psi$ with the boundary conditions that $\psi(-x_p) = 0$; $\psi(x_n) = V_{bi}$ (in respect to the p-side conduction band):

$$\psi(x) = \begin{cases} \frac{eN_a}{2\epsilon_0\epsilon_{sc}}(x + x_p)^2 & \text{for} \quad -x_p < x < 0 \\ \frac{e}{2\epsilon_0\epsilon_{sc}}\left(N_D x_n^2 + N_A x_p^2\right) - \frac{eN_D}{2\epsilon_0\epsilon_{sc}}(x - x_n)^2 & \text{for} \quad 0 < x < x_n \end{cases}$$

From this result we can deduce the depletion zone width $w = x_n + x_p$ in thermal equilibrium if we utilise the boundary condition $\psi(x_n) = V_{bi}$:

$$\begin{aligned} \psi(x_n) = \quad V_{bi} &= \frac{e(N_D x_n^2 + N_A x_p^2)}{\epsilon_{sc}\epsilon_0} \\ \Rightarrow \quad V_{bi} &= \frac{eN_D^2}{2\epsilon_{sc}\epsilon_0} x_n^2 N_j^{-1} = \frac{eN_A^2}{2\epsilon_{sc}\epsilon_0} x_p^2 N_j^{-1} \end{aligned}$$

Here we have used $E_{max} = \frac{eN_d x_n}{\epsilon_0\epsilon_{sc}} = \frac{eN_a x_p}{\epsilon_0\epsilon_{sc}}$ and $N_j^{-1} \doteq N_A^{-1} + N_D^{-1}$. Thus we can rewrite this relation to obtain x_n and x_p:

$$x_n = \frac{1}{N_D}\sqrt{\frac{2\epsilon_0\epsilon_{sc}N_j V_{bi}}{e}} \; ; \; x_p = \frac{1}{N_A}\sqrt{\frac{2\epsilon_0\epsilon_{sc}N_j V_{bi}}{e}} \qquad \text{(A.1)}$$

$$w = x_n + x_p = \sqrt{\frac{2\epsilon_0\epsilon_{sc}V_{bi}}{N_j e}}$$

For pos. forward bias[2] the potential is changed: $V_{bi} \longmapsto V_{bi} - V_{fwd}$. We can see how x_n, x_p change with the doping levels N_D & N_A.

A.3 Drift & Diffusion across unbiased p-n Junctions

When p- and n-type material are brought in contact to form a junction majority carriers feel the carrier density gradient to the other material respectively. Thus they abandon their dopant sites and travel across the junction leaving behind un-compensated donors/acceptors which will cause a field to build up inhibiting further flow of carriers across the interface. This zone of un-compensated dopants near the interface is assumed to be devoid of free carriers as eventually an equilibrium will be reached where the electric field totally inhibits the diffusive current along the concentration gradient:

$$\begin{aligned} \vec{j}_n = & \quad en \overbrace{\mu_n \vec{E}}^{v_n^{drift}} + eD_n \vec{\nabla} n \quad = 0 \Rightarrow \frac{\mu_n \vec{E} dx}{D_n} = -\frac{dn}{n} \\ \vec{j}_p = & \quad en \underbrace{\mu_p \vec{E}}_{v_p^{drift}} - eD_p \vec{\nabla} p \quad = 0 \Rightarrow \frac{\mu_p \vec{E} dx}{D_p} = \frac{dp}{p} \end{aligned}$$

The carrier concentrations are n and p; μ and D are carrier mobilities and diffusion constants for the two carrier types. Using $\vec{E} = -\vec{\nabla}\phi$, $E = q\phi$ and $n = n_i e^{e(\phi_F - \phi)/KT}$ we can rewrite $\vec{j}_n$ as $\vec{j}_n = -en\mu_n \vec{\nabla}\phi_F^i - eD_n \frac{en}{KT}[\vec{\nabla}\phi - \vec{\nabla}\phi_F] = 0$ shows us the alignment of the two Fermi levels ($\vec{\nabla}\phi_F = 0$) as $\vec{\nabla}\phi$ must be zero to cancel out the rapid change in n across the junction.

Although the abovementioned relations are three dimensional they assume homogeneity across the whole junction which reduces the problem to a quasi one-dimensional one.

Einstein Relation From the current densities above we can derive a relation between carrier mobilities and diffusion constants[3]. Introducing a spatially variable

[2] as always this applies to neg. backward bias as well
[3] shown only for electrons, holes corresponding

donor potential $\Phi(x)$ results in a changed density of carriers

$$n_{cb}(x) = 2h^{-3}(2\pi m_e^* KT)^{3/2} \cdot \exp -\frac{E - e\Phi(x) - E_F}{KT}$$

$$\Rightarrow \quad \vec{j}_n = en(x)\mu_n \vec{E} + eD_n \vec{\nabla} n(x) = 0 = en(x)\mu_n \vec{E} - e\frac{eD_n}{KT} n(x)\vec{E}$$

We end up with $\mu_n = \frac{eD_n}{KT} \& \mu_p = -\frac{eD_p}{KT}$, the Einstein relations.

Making use of the last result we rewrite the relations derived from the current densities and integrate over the depletion region with boundaries $-x_p$, x_n:

$$-\frac{eE}{KT}dx = \frac{dn}{n} = \frac{dp}{p} = -\frac{e}{KT}dV$$

$$\Rightarrow \quad \int_{n_p}^{n_n} \frac{dn}{n} = \int_{p_p}^{p_n} \frac{dp}{p} = \int_{-x_p}^{x_n} -\frac{e}{KT}dV$$

$$\Rightarrow \quad n_p = n_n \cdot e^{-\frac{eV_{bi}}{KT}} \; ; \; p_n = p_p \cdot e^{-\frac{eV_{bi}}{KT}}$$

A.4 Recombination at the Depletion Zone Boundary

Minority carriers injected across the junction barrier recombine with a recombination time τ after crossing the depletion zone boundary (DZB) as they encounter majority carriers there. Accounting for charge conservation we get for electrons[4]:

$$\vec{\nabla} j - e\frac{n_p(x) - n_{p0}}{\tau_n} = e\frac{dn}{dt}$$

$$\text{with} \quad \vec{j} = eD_n \vec{\nabla} n - en\mu_n \vec{\nabla}\phi = eD_n \vec{\nabla} n \quad \text{as } \vec{E} = 0 \text{ at DZB}$$

$$\overset{equil.}{\Rightarrow} \quad D_n \cdot \vec{\nabla}^2 n_p(x) = \frac{n_p(x) - n_{p0}}{\tau_e}$$

Using the boundary condition that the injected carries at DZB are $n_p(x = -x_p) = n_{p0} + n_{p0} \cdot [\exp \frac{eV_{fwd}}{KT}]$ (which assumes that the diffusion length is shorter than the distance to a surface) we can solve this differential equation:

$$n_p(x) = n_{p0} + n_{p0} \cdot \left[e^{\frac{eV_{fwd}}{KT}} - 1 \right] \cdot e^{\frac{x + x_p}{\sqrt{\tau_e D_n}}}$$

Tagging $\sqrt{\tau_e D_n}$ as a recombination scope L_n is natural; the same steps apply for minority holes.

[4] and correspondingly for holes

APPENDIX B

Fresnel Coefficients

Using Maxwell's equations on the problem of a semiconductor-air interface and applying boundary conditions for field continuity yields Fresnel's coefficients for electro-magnetic transmission and reflection of TE and TM polarisation:

$$r_{TE} = -\frac{\sin(\theta_i - \theta_t)}{\sin(\theta_t + \theta_i)} \quad ; \quad t_{TE} = \frac{2\sin\theta_t \cos\theta_i}{\sin(\theta_t + \theta_i)}$$
$$r_{TM} = \frac{\tan(\theta_i - \theta_t)}{\tan(\theta_t + \theta_i)} \quad ; \quad t_{TM} = \frac{2\sin\theta_t \cos\theta_i}{\sin(\theta_t + \theta_i)\cos(\theta_i - \theta_t)}$$

The angle of incidence (and reflection) measured to the normal is denoted θ_i while θ_t is the angle to the interface normal for the transmitted intensity. TE polarisation is defined as the electric field lying in the plane spanned up by the normal to the interface and the direction the electro-magnetic wave travels while for TM it's the magnetic field doing so.

For a non-absorptive medium we can now write for the reflected and transmitted electro-magnetic field intensities $I = \left(\vec{E}_0 \cdot \exp i(kx - \omega t)\right)^2 = E_0^2$ of the two polarisations:

$$I_{TE} = r_{TE}^2 \cdot I_{TE} + t_{TE}^2 \cdot I_{TE} \quad ; \quad I_{TM} = r_{TM}^2 \cdot I_{TM} + t_{TM}^2 \cdot I_{TM}$$

or for short $\mathcal{R}_{TE/TM} + \mathcal{T}_{TE/TM} = 1$ which expresses energy conservation as the Poynting vector is proportional to I. If the material is absorptive, energy conservation changes this to:

$$\mathcal{R}_{TE/TM} + \mathcal{T}_{TE/TM} + \mathcal{A}_{TE/TM} = 1 \tag{B.1}$$

.

APPENDIX C

Free Carrier Absorption

In semiconductors doped above the metal-insulator transition carriers are nominally free and absorb energy from an applied field as they experience its acceleration. Free carriers (in our case electrons for n-doped material) obey the following equation of motion under the influence of an oscillating electric field $E = E_0 e^{-i\omega t}$ with $v = \frac{dx}{dt}$, μ the carrier mobility, and τ the carrier relaxation time ($\tau = \frac{m^* \mu}{e}$):

$$\begin{aligned} & m^* \left(\tfrac{d^2x}{dt^2} + \tfrac{v}{\tau} \right) = e \cdot E_0 e^{-i\omega t} \quad | \cdot ne \\ \Rightarrow \qquad & \tfrac{dj}{dt} + \tfrac{j}{\tau} = \tfrac{e^2 n}{m^*} \cdot E_0 e^{-i\omega t} \end{aligned}$$

On the assumption that j is of the form $j = j_0 e^{-i\omega t}$ and $\gamma \doteq \tau^{-1}$ it follows that:

$$\begin{aligned} & (-i\omega + \gamma) \cdot j_0 = \tfrac{e^2 n}{m^*} \cdot E_0 \\ \Rightarrow \qquad & j_0 = \tfrac{e^2 n}{m^*(-i\omega+\gamma)} \cdot E_0 \end{aligned}$$

Making use of Maxwell's equations we relate electric field $\vec{E}$ and current density as follows (μ_0 and c defined as canonical):

$$\begin{aligned} & \vec{\nabla} \times \vec{E} = -\tfrac{\partial \vec{B}}{\partial t} \;\Rightarrow\; \vec{\nabla} \times \left(\vec{\nabla} \times \vec{E} \right) = -\tfrac{\partial}{\partial t} \left(\vec{\nabla} \times \vec{B} \right) \\ \Rightarrow \qquad & \vec{\nabla} \underbrace{(\vec{\nabla} \vec{E})}_{=\,0 \text{ as } \rho\,=\,0} - \Delta \vec{E} = -\tfrac{\partial}{\partial t} \left(\mu_0 \vec{j} + \tfrac{1}{c^2} \tfrac{\partial \vec{E}}{\partial t} \right) \\ \Rightarrow \qquad & \Delta \vec{E} = \mu_0 \tfrac{\partial \vec{j}}{\partial t} + \tfrac{1}{c^2} \tfrac{\partial^2 \vec{E}}{\partial t^2} \end{aligned}$$

On the assumption that $\vec{E}$ has the form $\vec{E}(x,t) = \underbrace{\vec{E}_0}_{\text{const.}} \cdot e^{i(kx - \omega t)}$ and $\vec{j}$ accordingly we can solve this partial differential equation:

$$\begin{aligned} & -k^2 \vec{E} = -\mu_0 i\omega \vec{j} - \tfrac{1}{c^2} \omega^2 \vec{E} \\ \Rightarrow \qquad & k^2 = \mu_0 i\omega \tfrac{e^2 n}{m^*(-i\omega+\gamma)} + \tfrac{\omega^2}{c^2} \qquad \text{with } c^2 = \frac{1}{\mu_0 \epsilon_0} \\ \Rightarrow \qquad & k^2 = \tfrac{\omega^2}{c^2} \left(\tfrac{i e^2 n}{m^* \epsilon_0 \omega} \tfrac{1}{(-i\omega+\gamma)} + 1 \right) \end{aligned}$$

As $k^2 = \frac{\omega^2}{c^2} \cdot \hat{n}^2$ we can deduce the complex refractive index $\hat{n} \doteq n + i\kappa$ to be

$$\hat{n}^2 = \left(1 + \frac{ie^2 n}{m^* \epsilon_0 \omega} \frac{1}{(-i\omega + \gamma)}\right) \tag{C.1}$$

, so that the complex susceptibility $\hat{\epsilon} = \hat{n}^2 \doteq \epsilon_1 + i \cdot \epsilon_2$ is:

$$\hat{\epsilon} = \left(1 + \frac{ie^2 n(\gamma + i\omega)}{m^* \epsilon_0 \omega} \frac{1}{(\gamma^2 + \omega^2)}\right)$$

Using the relations $\gamma = \tau^{-1}$ and $\sigma_{dc} = \frac{ne^2\tau}{m^*}$ we can rewrite the real and complex parts of $\hat{\epsilon}$ as:

$$\begin{aligned} \epsilon_1 &= \left(1 + \frac{e^2 n}{m^* \epsilon_0} \frac{1}{(\gamma^2 + \omega^2)}\right) = \left(1 - \frac{\sigma_{dc}\tau}{\epsilon_0(1 + \omega^2\tau^2)}\right) \\ \epsilon_2 &= \left(\frac{e^2 n\gamma}{m^* \epsilon_0 \omega(\gamma^2 + \omega^2)}\right) = \left(\frac{\sigma_{dc}}{\epsilon_0 \omega(1 + \omega^2\tau^2)}\right) \end{aligned}$$

This could be rewritten yet again using the definition of ω_p, the plasma frequency ($\omega_p^2 = \frac{nq^2}{m\epsilon_0}$), so that $\sigma_{dc} = \frac{nq^2\tau}{m^*} = \epsilon_0 \tau \omega_p^2$. This result will now be used to obtain expressions for the actual real refractive index n and, more importantly for our aim to understand free carrier absorption, the extinction coefficient κ:

$$\begin{aligned} & \hat{n}^2 = n^2 + 2in\kappa - \kappa^2 = \epsilon_1 + i\epsilon_2 = \hat{\epsilon} \;\Rightarrow\; \epsilon_1 = n^2 - \kappa^2 \;;\; \epsilon_2 = 2n\kappa \\ \Rightarrow \quad & n^2 - \kappa^2 = \left(1 - \tfrac{\sigma_{dc}\tau}{\epsilon_0(1+\omega^2\tau^2)}\right) \;;\; 2n\kappa = \left(\tfrac{\sigma_{dc}}{\epsilon_0\omega(1+\omega^2\tau^2)}\right) \\ \Rightarrow \quad & n = \tfrac{\sigma_{dc}}{2\kappa\epsilon_0\omega(1+\omega^2\tau^2)} \end{aligned}$$

As $k = \frac{\omega}{c}(n + i\kappa)$ we finally end up with the result for the absorption coefficient α due to absorption by free carriers:

$$E = E_0 \cdot e^{i(\frac{w}{c}nx - wt) - 2\kappa\frac{\omega}{c}\cdot x/2}$$

$$\text{with} \quad \alpha \doteq 2\kappa\tfrac{\omega}{c} = \tfrac{\sigma_{dc}}{nc\epsilon_0(1+\omega^2\tau^2)} \overset{\omega\tau\sim eq}{\sim} \underbrace{(c\epsilon_0)^{-1}}_{376.7\Omega} \cdot \tfrac{\sigma_{dc}}{n\omega^2\tau^2} \overset{\sigma=ne\mu}{=} \tfrac{1}{c\epsilon_0} \cdot \tfrac{e\mu}{(\omega\tau)^2} \tag{C.2}$$

References

[Barnes, 1994] Barnes, J. M. (1994). *An experimental and theoretical Study of GaAs/InGaAs Quantum Well Solar Cells and Carrier Escape from Quantum Wells.* PhD dissertation, University of London, Physics Department, Imperial College of Science, Technology and Medicine, London.

[Barnham et al., 1994] Barnham, K. W. J. et al. (1994). Quantum well solar cells. *Optoelectronics - Devices and Technologies*, 9(4):483–498.

[Barnham et al., 1996] Barnham, K. W. J. et al. (1996). Voltage enhancement in QWSC's. *Journal of Applied Physics*. submitted in December 1995.

[Brendel et al., 1996] Brendel, R., Werner, J. H., and Queisser, H. J. (1996). Thermodynamic efficiency limits for semiconductor solar-cells with carrier multiplication. *Solar Energy Materials and Solar Cells*, 41(2):419–425.

[Grätzel and Bonhôte, 1994] Grätzel, M. and Bonhôte, P. (1994). Development of a new type of solar cell based on sensitized, nanocrystalline, semiconducting films. Available from Ecole Polytechnique fédérale de Lausanne, Institut de chimie physique II, CH-1015 Lausanne.

[Green, 1987] Green, M. A. (1987). *High Efficiency Si Solar Cells.* Aedermannsdorf, first edition. ISBN 0-87849-537-1.

[Green et al., 1996] Green, M. A., Emery, K., Bücher, K., and King, D. L. (1996). Solar cell efficiency tables (version 7). *Progress in Photovoltaics: Research and Applications*, 4:59–62.

[Nelson, 1995] Nelson, J. (1995). Quantum-well structures for photovoltaic energy conversion. *Thin Films*, 21:311–368.

[Spitzer and Whelan, 1959] Spitzer, W. G. and Whelan, J. M. (1959). Infrared absorbtion and electron effective mass in n-type gallium arsenide. *Physical Review*, 114(1):59–63.

[Sze, 1981] Sze, S. M. (1969c1981). *Physics of Semiconductor Devices*. John Wiley & Sons, Inc., 603 Third Avenue, New York, New York 1058, second edition. ISBN 0-471-05661-8.

[Yablonovitch and Cody, 1984] Yablonovitch, E. and Cody, G. D. (1984). Intensity enhancement in textured optical sheets for solar cells. *IEEE Transactions on Electron Devices*, ED-29:634–636.

[Zachariou et al., 1996] Zachariou, A., Barnham, K. W. J., et al. (1996). A new approach to p-doping and the observation of efficiency enhancement in $InP/InGaAs$ QWSC's. In *Proceedings 25th IEEE Photovolatic Specialists Conference*, number 25 in IEEE Photovolatic Specialists Conferences, Washington. IEEE.